ADVANCES IN PHYSICS, 2003, VOL. 52, NO. 4, 343–383

Taylor & Francis
Taylor & Francis Group

Dielectric electrorheological fluids: theory and experiment

HONGRU MA,* WEIJIA WEN, WING YIM TAM and PING SHENG†
Department of Physics, Hong Kong University of Science and Technology, Hong Kong, PR China

[Received 12 September 2001; revised 2 September 2002; accepted 29 October 2002]

Abstract

Electrorheological (ER) fluids are a class of materials whose rheological properties are controllable by the application of an electric field. A dielectric electrorheological (DER) fluid is the simplest type of ER fluid, in which the material components follow a linear electrostatic response. We review and discuss the progress of the studies on physics of this type of material. A first-principles theory of DER fluids, along with relevant experimental verifications, are presented in some detail. In particular, the properties presented include static equilibrium structure, shear modulus, static yield stress and its variation with applied electric field frequency, and structure-induced dielectric nonlinearity.

Contents PAGE

* Permanent address: Institute of Theoretical Physics, Shanghai Jiao Tong University, Shanghai 200240, PR China.
† Author for correspondence. e-mail: sheng@ust.hk

Advances in Physics ISSN 0001–8732 print/ISSN 1460–6976 online
http://www.tandf.co.uk/journals
DOI: 10.1080/0001873021000059987

1. Introduction

Electrorheological (ER) fluids are a class of materials whose rheological properties are controllable by the application of an electric field. During the past two decades, there has been a renewed interest in ER fluids research. The understanding of the ER mechanism, and the search for better ER materials, are the focus of much theoretical and experimental study [1–4].

It is the purpose of this paper to review studies on the physics of the simplest type of ER fluid: uniformly sized, solid dielectric spheres dispersed in a liquid. Both the solid and the liquid components are assumed to follow a linear electrostatic response under an applied field (although the composite system may not, as seen below). We denote this type of ER fluid as a dielectric electrorheological (DER) fluid.

A heuristic picture of the ER mechanism may be stated as follows. Due to the dielectric constant contrast between the solid particles and the liquid, each solid particle is polarized under an electrostatic field, with an effective dipole moment. The resulting dipole–dipole interaction means that the particles tend to aggregate and form columns along the applied field direction, with a microstructure inside the columns predictable from the dipole–dipole interaction [5]. However, such a picture leaves many questions unanswered. For example, multipole interactions are necessarily important as the particles are in close contact with each other in the aggregated state. Moreover, local fields should be properly taken into account. These two considerations make accurate simulations very difficult. In addition, the heuristic picture takes into account only the difference in the real part of the solid and liquid dielectric constants, whereas in reality some finite imaginary part in the dielectric constants may exist due to conductivity and/or relaxational effects. The physical implications of the imaginary part of the dielectric constant, and how they can be calculated, are important questions for the realistic prediction of DER fluid properties.

In this article, a first-principles investigation of DER fluids is presented as the unifying theme, under which the relevant literature is reviewed. By formulating the search for ground state configuration in terms of effective dielectric constant maximization, the free energy density of the system has been calculated via the Bergman–Milton representation [6–8]; multipole interaction, local field, and the contribution from the imaginary part of the dielectric constant are thereby accurately accounted for. Delineation of a shear distortion path from the ground state configuration leads directly to the definition of the shear modulus and the static yield stress of DER fluids. As a by-product, we give the upper bounds for the shear modulus and the static yield stress, quantities important for potential applications. From an intuitive understanding of the upper bounds we propose an optimal structure for the solid spheres that maximizes the yield stress. Perhaps it is equally important to note that the topic of dynamic yield stress is beyond the scope of the present work, but in the literature there have been many simulations on the dynamic aspects of DER fluids.

Bonnecaze and Brady [9, 10] have formulated a theory incorporating the dynamics of both fluid and solid particles. Simulations based on this formulation were performed on systems consisting of 25 or 49 particles, in two spatial dimensions. Klingenberg *et al.* [11–14] carried out simulations based on the interaction of point dipoles with hard core repulsion, coupled with Stokes hydrodynamic drag on the particles. They studied the rheology and kinetics of structure formation in DER fluids. Hass [15] performed simulations excluding the Brownian

force, and analysed the structure formation from his data. Similar studies were also performed by Tao's group [16, 17], and Wang *et al.* [18, 19]. Hu *et al.* [20] did simulations by considering the torque on solid particles and, based on a simple model, partly included the two-body hydrodynamic interactions. Conrad and coworkers [21–26] have developed model theories along with their experimental studies.

The paper is organized as follows. General formulation of the DER fluids model in section 2 is followed by a more detailed exposition of the relevant theoretical tools in section 3. In section 4 we present the results for the optimal ground state structure of DER fluids. Delineation of the shear distortion, and calculation of the shear modulus and yield stress, are presented in section 5. In section 6 we give the upper bounds to the shear modulus and yield stress, and propose an optimal coating structure for the solid spheres that can maximize the yield stress. In section 7 we present experimental results to compare with the theoretical predictions, and show that the frequency (of the applied electric field) dependence of the yield stress may be accounted for by the Debye relaxation effect in solid dielectric particles. We conclude with a few remarks on prospects for future research. Technical details of the theory are given in the appendices.

2. Formulation

In ER fluids, the operating frequency of the applied electric field is generally less than 10 kHz; thus the relevant electromagnetic wavelength is larger than a few kilometres. Comparison with the size of ER particles and their separations, which are almost always less than 10 microns, means that the ER fluid system is firmly in the so-called long wavelength, or electrostatic limit. It is the purpose of the present formulation to focus on the equilibrium state of DER fluids and their associated properties. Hence the dynamic process of structure formation is beyond the scope of the following discussion. The response of the system to an external electric field is therefore completely captured by a 3×3 effective dielectric constant tensor,

$$\tilde{\varepsilon}_{eff} = \begin{pmatrix} \bar{\varepsilon}_{xx} & \bar{\varepsilon}_{xy} & \bar{\varepsilon}_{xz} \\ \bar{\varepsilon}_{yx} & \bar{\varepsilon}_{yy} & \bar{\varepsilon}_{yz} \\ \bar{\varepsilon}_{zx} & \bar{\varepsilon}_{zy} & \bar{\varepsilon}_{zz} \end{pmatrix},$$

where each matrix element is a complex number, with the imaginary part denoting the conductivity or relaxational effect. The Gibbs free energy density f of the system is given by [27, 28]

$$f = -\frac{1}{8\pi}\mathbf{E} \cdot \mathrm{Re}(\tilde{\varepsilon}_{eff}) \cdot \mathbf{E} - TS, \tag{2.1}$$

where Re( ) means the real part of the quantity in the parentheses, T denotes temperature, S the entropy, and $\mathbf{E} = \Delta V/\ell$ the externally applied electric field, assumed to be in the z direction, with ΔV the voltage difference across the sample and ℓ the sample thickness. In equation (2.1) and those that follow, electrostatic units (esu) are used. In this work, we consider only those cases where spheres in the DER fluids are larger than a few microns, and/or the electric field is large (the first term on the right-hand side of (2.1) is much larger than the second term), i.e. the high field state. In these cases the entropy effect due to Brownian motion of the particles is negligible. Hence the free energy density may be written as

$$f = -\frac{1}{8\pi}\mathrm{Re}\,(\bar{\varepsilon}_{zz})\mathbf{E}^2. \tag{2.2}$$

Equation (2.2) follows directly from the first term on the right-hand side of equation (2.1) if the electric field direction is defined to be the z direction. In this case the electric field defines one of the principal directions of the dielectric tensor, hence only one element of the tensor appears in (2.2).

As the physical system is governed by the principle of minimum free energy, the search for the high field ground state of the DER fluid is thereby transformed to an optimization problem where the real part of $\bar{\varepsilon}_{zz}$ is maximized with respect to the positions of the solid spheres. It should be noted that due to the microstructure change associated with this optimization process, the effective dielectric constant tensor of the ER fluid system is necessarily nonlinear. That is, $\tilde{\varepsilon}_{eff}$ varies as a function of $\mathbf{E}$. This fact has been experimentally demonstrated [29], as presented below.

The search for the high field ground state may be limited to periodic structures, which follows from the plausible assumption that, for the ground state, the local microstructure should be unique. From physical considerations, the body-centred tetragonal (BCT) structure and the face-centred cubic (FCC) are good candidates. The former is formed by chains of spheres aligned along the z direction, where each chain (the central chain) is surrounded by four neighbouring chains shifted by one radius (in the z direction) from the central chain. This structure has the advantage that a chain of spheres is clearly the lowest energy state for polarized dipoles. The one radius shift between the nearest neighbour chains (while maintaining sphere–sphere contacts between the neighbouring chains) makes the angle between the centres of two neighbouring chain spheres 60°. While this angle is slightly larger than the magic angle of 54.7° for the dipole–dipole interaction (where the sign of interaction changes), a more accurate calculation, taking into account other than the nearest neighbours and dipole interactions, shows the chain–chain interaction to be weakly attractive, thus further reducing the energy. The FCC structure has the advantage that it has the highest packing density. Besides the BCT and FCC, in the following we also consider the body-centred cubic (BCC), the hexagonal close-packed (HCP), and the diamond structures. It will be shown that the BCT structure is indeed the ground state, but the difference in energy from the FCC is very small. We also show below that FCC and HCP have almost the same free energy to within the accuracy of calculation.

The elastic moduli of a crystal are usually defined by distortions from the ground state. In the case of the high field (HF) ground state of the ER fluid, however, the compressional modulus is generally ill defined. That is because in the HF ground state, each solid sphere experiences an inward compressional electrostatic pressure from neighbouring spheres, which is counterbalanced by steric repulsion between the spheres. Therefore if only the electrostatic part of the energy density is considered, the system would not be in the force-balance state. Hence it is not possible to define a compressional modulus by considering only the electrostatic energy density. The situation is different for the shear modulus and the static shear yield stress, because it is possible to define a shear distortion path whereby the spheres remain in contact with each other. From the calculated shear stress versus the shear strain curve, one can directly evaluate the shear modulus as the initial linear slope of the stress–strain relation, and the yield stress from the peak position of the same. The yield stress so

obtained is defined as the static yield stress, to be distinguished from the dynamic yield stress which involves ER fluid dynamics. We show that in the presence of water or conducting ions, the static yield stress can vary as a function of applied electric field frequency, generally decreasing as the frequency increases beyond a few hundred hertz.

It should be noted that a significant difference between the HF-ER fluid solid and the usual atomic solids is that the yield stress of an ordinary solid is generally related to the dislocation density and other imperfections, whereas in ER fluids we find good agreement between the experimental static yield stress and that calculated from shear distortion from the ground state, as described above.

3. Effective dielectric constant evaluation

The formulation of the DER fluid problem shows the evaluation of the effective dielectric constant to be an essential element. Here the various effective medium theories are inapplicable, since they do not account for the microstructural details of the system, which are vital in our case. We therefore use the exact theory of the Bergman–Milton representation [6–8] to calculate $\bar{\varepsilon}_{zz}$. In this formulation we will use the principal axes of the dielectric tensor as our coordinates so that we need to calculate only the diagonal elements of the dielectric tensor.

Consider n grains with dielectric constants ε_i, $i = 1, 2, 3, \ldots, n$, embedded in a liquid matrix with dielectric constant ε_ℓ. The multi-component formulation is necessary because we consider dielectric spheres coated with different types of materials, i.e. multiply-coated microspheres. The spatially varying dielectric constant of the system can be written as

$$\varepsilon(\mathbf{r}) = \varepsilon_\ell \left(1 - \frac{1}{s_1}\eta_1(\mathbf{r}) - \frac{1}{s_2}\eta_2(\mathbf{r}) - \cdots - \frac{1}{s_n}\eta_n(\mathbf{r}) \right), \tag{3.1}$$

where

$$s_i = \frac{\varepsilon_\ell}{\varepsilon_\ell - \varepsilon_i} \tag{3.2}$$

are complex numbers which constitute the materials input to the problem. $\eta_i(\mathbf{r})$ is the characteristic function, defined as

$$\eta_i(\mathbf{r}) = \begin{cases} 1 & \text{in the region of } \varepsilon_i, \\ 0 & \text{otherwise.} \end{cases} \tag{3.3}$$

The static electric potential is the solution of the following equation

$$\nabla \cdot (\varepsilon(\mathbf{r}) \nabla \phi(\mathbf{r})) = 0. \tag{3.4}$$

The boundary condition of the problem is given by (with unit electric field)

$$\phi(x, y, z = 0) = 0,$$

$$\phi(x, y, z = \ell) = \ell. \tag{3.5}$$

Here $\ell \to \infty$ in actual calculations. It is perhaps instructive to note here that in ER fluid systems, the metallic electrodes not only apply the electric field, but also serve to reduce the depolarization field effect through the image dipoles. As the same is not

true for magnetorheological systems, the magnetic depolarization effect is a major element to be considered.

We first consider the solution of equation (3.4) in the case of only one type of grain. In this case the dielectric constant of the system, equation (3.1), becomes

$$\varepsilon(\mathbf{r}) = \varepsilon_\ell\left(1 - \frac{1}{s}\eta(\mathbf{r})\right), \tag{3.6}$$

where the material characteristics of the problem are contained in the complex parameter

$$s = \frac{\varepsilon_\ell}{\varepsilon_\ell - \varepsilon_1}, \tag{3.7}$$

whereas the microstructure is implied by the indicator function

$$\eta(\mathbf{r}) = \begin{cases} 1 & \text{in the region of } \varepsilon_1 \\ 0 & \text{otherwise.} \end{cases} \tag{3.8}$$

The physical value of s cannot lie in the interval of $[0, 1]$ on the real axis, because when ε_ℓ and ε_1 are both real, s has to be less than zero or greater than 1. If one or both were complex, then s is away from the real axis unless ε_ℓ and ε_1 are proportional. In that case the proportionality constant must be positive, since otherwise one of the imaginary parts of the dielectric constants would be negative and hence unphysical. This requirement renders s to be outside the interval $[0, 1]$. This property of the material parameters is important in later discussions.

Substitution of equation (3.6) into (3.4) yields

$$\nabla^2\phi(\mathbf{r}) = \frac{1}{s}\nabla\cdot(\eta(\mathbf{r})\nabla\phi(\mathbf{r})). \tag{3.9}$$

By regarding the right-hand side of equation (3.9) as the source term, we may solve for $\phi(\mathbf{r})$ by using Green's function, whereby the solution can be written as a sum of two parts: the solution of the homogeneous Laplace equation which satisfies the boundary conditions ($\phi_0 = E_0 z = z$ in our problem, as $E_0 = 1$ by definition), plus the integral of the Green's function of the Laplacian

$$G(\mathbf{r}, \mathbf{r}') = \frac{1}{4\pi|\mathbf{r} - \mathbf{r}'|}, \tag{3.10}$$

multiplied by the source term. That is,

$$\phi(\mathbf{r}) = z - \frac{1}{s}\int \mathrm{d}V' G(\mathbf{r}, \mathbf{r}')\nabla'\cdot(\eta(\mathbf{r}')\nabla'\phi(\mathbf{r}')). \tag{3.11}$$

The second term on the right-hand side of equation (3.11) can be rewritten through integration by parts:

$$\phi = z + \frac{1}{s}\int \mathrm{d}V'\eta(\mathbf{r}')\nabla' G(\mathbf{r}, \mathbf{r}')\cdot\nabla'\phi(\mathbf{r}'). \tag{3.12}$$

We define a linear integral operator $\hat{\Gamma}$ as

$$\hat{\Gamma}\phi(\mathbf{r}) \equiv \int \mathrm{d}V'\eta(\mathbf{r}')\nabla' G(\mathbf{r}, \mathbf{r}')\cdot\nabla'\phi(\mathbf{r}'). \tag{3.13}$$

In terms of $\hat{\Gamma}$, equation (3.12) can be written in a more compact form as

$$\phi = z + \frac{1}{s}\hat{\Gamma}\phi. \tag{3.14}$$

The operator $\hat{\Gamma}$ is Hermitian under the following definition of the inner product:

$$\langle\psi|\phi\rangle = \int \mathrm{d}V \eta(\mathbf{r}) \nabla\psi^*(\mathbf{r}) \cdot \nabla\phi(\mathbf{r}). \tag{3.15}$$

To prove this statement, it is simple to observe that

$$\begin{aligned}
\langle\psi|\hat{\Gamma}|\phi\rangle &\equiv \int \mathrm{d}V \eta(\mathbf{r}) \nabla\psi(\mathbf{r})^* \cdot \nabla\left(\int \mathrm{d}V' \eta(\mathbf{r}') \nabla' G(\mathbf{r}, \mathbf{r}') \cdot \nabla'\phi(\mathbf{r}')\right) \\
&= \int \mathrm{d}V \eta(\mathbf{r}) \int \mathrm{d}V' \eta(\mathbf{r}') \nabla\psi(\mathbf{r})^* \cdot \nabla\nabla' G(\mathbf{r}, \mathbf{r}') \cdot \nabla'\phi(\mathbf{r}') \\
&= \langle\phi|\hat{\Gamma}|\psi\rangle^*.
\end{aligned}$$

The eigenvalues of the operator $\hat{\Gamma}$ are therefore real. It can be further proved that all eigenvalues of the operator $\hat{\Gamma}$ are bounded in the interval $[0, 1]$ [6]. As the material parameter s cannot be in the interval $[0, 1]$, equation (3.14) can thus be inverted to give a formal solution of ϕ:

$$\phi = \left(1 - \frac{1}{s}\hat{\Gamma}\right)^{-1} z. \tag{3.16}$$

With this formal solution, we can now write down an expression for the effective dielectric constant which, by definition, is obtained as the ratio of the spatial average of the displacement vector **D** to the applied electric field. Since the applied electric field is in the z direction, the zz component of the effective dielectric constant can be written as

$$\overline{\varepsilon}_{zz} = \frac{1}{V}\int \mathrm{d}V[\varepsilon_\ell(1 - \eta(\mathbf{r})) + \varepsilon_1\eta(\mathbf{r})]\frac{\partial\phi(\mathbf{r})}{\partial z} = \varepsilon_\ell\left(1 - \frac{1}{V}\int \mathrm{d}V \frac{1}{s}\eta(\mathbf{r})\frac{\partial\phi(\mathbf{r})}{\partial z}\right). \tag{3.17}$$

The integral in equation (3.17) can be transformed to an inner product form defined by equation (3.15):

$$\begin{aligned}
\int \mathrm{d}V \eta(\mathbf{r})\frac{\partial\phi(\mathbf{r})}{\partial z} &= \int \mathrm{d}V \eta(\mathbf{r})\mathbf{e}_z \cdot \nabla\phi(\mathbf{r}) \\
&= \int \mathrm{d}V \eta(\mathbf{r}) \nabla z \cdot \nabla\phi(\mathbf{r}) \\
&= \langle z|\phi\rangle,
\end{aligned}$$

where $\mathbf{e}_z$ is the unit vector in the z direction. The effective dielectric constant can therefore be expressed as

$$\overline{\varepsilon}_{zz} = \varepsilon_l(1 - F(s)), \tag{3.18}$$

with

$$F(s) \equiv \frac{1}{V}\frac{1}{s}\langle z|\phi\rangle. \tag{3.19}$$

By using the formal solution of ϕ given in equation (3.16), (3.19) becomes

$$F(s) = \frac{1}{V}\frac{1}{s}\langle z|\phi\rangle$$
$$= \frac{1}{V}\langle z|(s-\hat{\Gamma})^{-1}|z\rangle$$
$$= \frac{1}{V}\sum_u \frac{|\langle z|\phi_u\rangle|^2}{s-s_u}, \tag{3.20}$$

where s_u and ϕ_u are, respectively, the (real) eigenvalues and eigenfunctions of operator $\hat{\Gamma}$. The last line of the equation (3.20) was obtained by inserting a completeness relation $\sum_u |\phi_u\rangle\langle\phi_u| = 1$ into the expression. In equation (3.20), the material parameter s and the geometric structure information, contained in s_u and ϕ_u, are clearly separated. Since s is a complex number, this separation affords a clear depiction of the effect of conductivity (or the imaginary part of the dielectric constants). Because the free energy (which must be real) is directly proportional to the real part of $\overline{\varepsilon}_{zz}$, equation (2.2), hence the structure, stress and other physical effects (derivable from the free energy) enter only through the real part of the effective $\overline{\varepsilon}_{zz}$. The imaginary part of $\overline{\varepsilon}_{zz}$ gives the overall dissipation of the system. In the expression for $\overline{\varepsilon}_{zz}$, since s_u and $|\langle z|\phi_u\rangle|^2$ are real numbers, it is clear from equation (3.20) that the imaginary part of the component dielectric constants (or s) do have a non-trivial contribution to the real part of (the effective) $\overline{\varepsilon}_{zz}$, and hence the ER effect.

Now we turn to the more general case of multi-component formulation. It is parallel to the simple case detailed above. Starting from equations (3.1) and (3.4), we obtain

$$\nabla^2\phi(\mathbf{r}) = \sum_{i=1}^{n}\frac{1}{s_i}\nabla\cdot(\eta_i(\mathbf{r})\nabla\phi(\mathbf{r})). \tag{3.21}$$

The solution of equation (3.21) with boundary conditions (3.5) can be formally written as:

$$\phi(\mathbf{r}) = z - \sum_{i=1}^{n}\frac{1}{s_i}\int \mathrm{d}V' G(\mathbf{r},\mathbf{r}')\nabla'\cdot(\eta_i(\mathbf{r}')\nabla'\phi(\mathbf{r}')). \tag{3.22}$$

Integration by parts yields

$$\phi = z + \sum_{i=1}^{n}\frac{1}{s_i}\int \mathrm{d}V'\eta_i(\mathbf{r}')\nabla' G(\mathbf{r},\mathbf{r}')\cdot\nabla'\phi(\mathbf{r}'). \tag{3.23}$$

We define linear integral operators $\hat{\Gamma}_i$, $i = 1, 2, \ldots, n$ as

$$\hat{\Gamma}_i\phi(\mathbf{r}) \equiv \int \mathrm{d}V'\eta_i(\mathbf{r}')\nabla' G(\mathbf{r},\mathbf{r}')\cdot\nabla'\phi(\mathbf{r}'). \tag{3.24}$$

In terms of $\hat{\Gamma}_i$, equation (3.23) can be written in a more compact form as

$$\phi = z + \sum_{i=1}^{n}\frac{1}{s_i}\hat{\Gamma}_i\phi. \tag{3.25}$$

The operator $\hat{\Gamma}_i$ is Hermitian under the following definition of the inner product:

$$\langle\psi|\phi\rangle_i = \int \mathrm{d}V \eta_i(\mathbf{r}) \nabla\psi^*(\mathbf{r}) \cdot \nabla\phi(\mathbf{r}), \tag{3.26}$$

because

$$\begin{aligned}\langle\psi|\hat{\Gamma}_i|\phi\rangle_i &\equiv \int \mathrm{d}V \eta_i(\mathbf{r}) \nabla\psi(\mathbf{r})^* \cdot \nabla\left(\int \mathrm{d}V' \eta_i(\mathbf{r}') \nabla' G(\mathbf{r},\mathbf{r}') \cdot \nabla'\phi(\mathbf{r}')\right) \\ &= \int \mathrm{d}V \eta_i(\mathbf{r}) \int \mathrm{d}V' \eta_i(\mathbf{r}') \nabla\psi(\mathbf{r})^* \cdot \nabla\nabla' G(\mathbf{r},\mathbf{r}') \cdot \nabla'\phi(\mathbf{r}') \\ &= \langle\phi|\hat{\Gamma}_i|\psi\rangle_i^*.\end{aligned}$$

The zz component of the effective dielectric constant can now be written as

$$\begin{aligned}\overline{\varepsilon}_{zz} &= \frac{1}{V}\int \mathrm{d}V \left[\varepsilon_\ell\left(1 - \sum_{i=1}^{n} \eta_i(\mathbf{r})\right) + \sum_{i=1}^{n} \varepsilon_i \eta_i(\mathbf{r})\right] \frac{\partial\phi(\mathbf{r})}{\partial z} \\ &= \varepsilon_\ell\left(1 - \frac{1}{V}\sum_{i=1}^{n} \int \mathrm{d}V \frac{1}{s_i} \eta_i(\mathbf{r}) \frac{\partial\phi(\mathbf{r})}{\partial z}\right).\end{aligned} \tag{3.27}$$

The integral in equation (3.27) can be transformed to an inner product form defined by equation (3.26):

$$\begin{aligned}\int \mathrm{d}V \eta_i(\mathbf{r}) \frac{\partial\phi(\mathbf{r})}{\partial z} &= \int \mathrm{d}V \eta_i(\mathbf{r}) \mathbf{e}_z \cdot \nabla\phi(\mathbf{r}) \\ &= \int \mathrm{d}V \eta_i(\mathbf{r}) \nabla z \cdot \nabla\phi(\mathbf{r}) \\ &= \langle z|\phi\rangle_i.\end{aligned}$$

Thus the effective dielectric constant can be written as

$$\overline{\varepsilon}_{zz} = \varepsilon_l(1 - F(s_1, s_2, \ldots, s_n)), \tag{3.28}$$

where

$$F(s_1, s_2, \ldots, s_n) = \frac{1}{V}\sum_{i=1}^{n} \frac{1}{s_i} \langle z|\phi\rangle_i. \tag{3.29}$$

From equation (3.29) we see that the potential itself is not needed if we are only interested in the evaluation of the effective dielectric constant. The only quantities required are the inner products $\langle z|\phi\rangle_i$. To establish a working procedure in the evaluation of these inner products, we expand the potential ϕ inside a grain in terms of the grain eigenfunctions, defined as

$$\hat{\Gamma}_i \phi_{iu}(\mathbf{r}) = s_{iu} \phi_{iu}(\mathbf{r}), \tag{3.30}$$

where s_{iu} and $\phi_{iu}(\mathbf{r})$ are the eigenvalues and eigenfunctions of $\hat{\Gamma}_i$.

The expansion of $\phi(\mathbf{r})$ inside the ith grain can be written as

$$\eta_i^+(\mathbf{r})\phi(\mathbf{r}) = \sum_u A_{iu} \eta_i^+(\mathbf{r}) \phi_{iu}(\mathbf{r}), \tag{3.31}$$

where A_{iu} denotes the expansion coefficients, and $\eta_i^+(\mathbf{r})$ is an indicator function which takes the value 1 both inside the grain i and in an infinitesimal shell on the

grain surface. The purposes of $\eta_i^+(\mathbf{r})$ are: (1) it limits the expansion only in the grains, and (2) it avoids the *delta* functions which will result from differentiations if $\eta_i(\mathbf{r})$ is used. From equation (3.25), we have inside the grain i

$$\eta_i^+(\mathbf{r})\phi(\mathbf{r}) = \eta_i^+(\mathbf{r})z + \eta_i^+(\mathbf{r})\int \mathrm{d}V'\nabla' G(\mathbf{r},\mathbf{r}')\cdot\sum_{j=1}^{n}\frac{1}{s_j}\eta_j(\mathbf{r}')\nabla'\phi(\mathbf{r}'). \tag{3.32}$$

Substitution of equation (3.31) into (3.32) leads to

$$\sum_u A_{iu}\eta_i^+(\mathbf{r})\phi_{iu}(\mathbf{r}) = \eta_i^+(\mathbf{r})z + \eta_i^+(\mathbf{r})\int \mathrm{d}V'\nabla' G(\mathbf{r},\mathbf{r}')\cdot\sum_{j=1}^{n}\frac{1}{s_j}\eta_j(\mathbf{r}')\nabla'\sum_v A_{jv}\eta_j(\mathbf{r}')\phi_{jv}(\mathbf{r}'). \tag{3.33}$$

By taking the gradient of both sides, multiplying by $\nabla\phi_{iu}^*$ and integrating, we obtain

$$\begin{aligned} A_{iu} &= z_{iu} + \sum_{j=1}^{n}\sum_v A_{jv}\frac{1}{s_j}\int \mathrm{d}V\eta_i(\mathbf{r})\nabla\phi_{iu}^*(\mathbf{r})\cdot\nabla\int \mathrm{d}V'\eta_j(\mathbf{r}')\nabla' G(\mathbf{r},\mathbf{r}')\cdot\nabla'\phi_{jv}(\mathbf{r}') \\ &= z_{iu} + \sum_{j=1}^{n}\sum_v A_{jv}\frac{1}{s_j}s_{jv}\int \mathrm{d}V\eta_i(\mathbf{r})\nabla\phi_{iu}^*(\mathbf{r})\cdot\nabla\phi_{jv}(\mathbf{r}). \end{aligned}$$

That is,

$$\sum_{j=1}^{n}\sum_v(\delta_{ij}\delta_{uv} - \frac{1}{s_j}\hat{\Gamma}_{iu,jv})A_{jv} = z_{iu}, \tag{3.34}$$

where

$$\hat{\Gamma}_{iu,jv} = s_{jv}\int \mathrm{d}V\eta_i(\mathbf{r})\nabla\phi_{iu}^*(\mathbf{r})\cdot\nabla\phi_{jv}(\mathbf{r}). \tag{3.35}$$

The effective dielectric constant may be represented as

$$\begin{aligned} \overline{\varepsilon}_{zz} &= \varepsilon_\ell\left(1 - \frac{1}{V}\sum_{i=1}^{n}\frac{1}{s_i}\int \mathrm{d}V\eta_i(\mathbf{r})\frac{\partial\phi(\mathbf{r})}{\partial z}\right) \\ &= \varepsilon_\ell\left(1 - \frac{1}{V}\sum_{i=1}^{n}\sum_u\frac{1}{s_i}A_{iu}\int \mathrm{d}V\eta_i(\mathbf{r})\frac{\partial\phi_{iu}(\mathbf{r})}{\partial z}\right) \\ &= \varepsilon_\ell\left(1 - \frac{1}{V}\sum_{i=1}^{n}\sum_u\frac{1}{s_i}A_{iu}z_{iu}\right). \end{aligned}$$

In the above equations, we have used the definition

$$z_{iu} \equiv \int \mathrm{d}V\eta_i\frac{\partial\phi_{iu}(\mathbf{r})}{\partial z}.$$

In the following we concentrate on grains of spherical shape, i.e. dielectric spheres, singly or doubly coated. In these cases the basic building blocks are spheres

and spherical shells. The eigenvalues and eigenfunctions for this type of geometry can be obtained analytically. Details are given in appendix A.

When the spheres form periodic structures, the above formulae can be further simplified for practical computation. Suppose the spheres are located on a lattice whose translation vector is given by $\mathbf{R}$, then we can rewrite equation (3.34) in the following explicit form:

$$\sum_{k'=1}^{3}\sum_{\mathbf{R}'}\sum_{l'm'p'}\left(\delta_{\mathbf{R}\mathbf{R}'}\delta_{kk'}\delta_{ll'}\delta_{mm'}\delta_{pp'}-\frac{1}{s_{k'}}\hat{\Gamma}_{klmp,k'l'm'p'}(\mathbf{R}-\mathbf{R}')\right)A_{k'l'm'p'}(\mathbf{R}')=z_{klmp}(\mathbf{R}). \tag{3.36}$$

Here k and k' can take values 1, 2 and 3, denoting the inner core, first shell and second shell, respectively; lm and $l'm'$ are indices of spherical harmonics, p and p' can be + or − corresponding to the two branches of eigenvalues and eigenfunctions of the spherical shell.

By defining the lattice Fourier transform

$$A_{klmp}(\mathbf{R})=\sum_{\mathbf{K}}A_{klmp}(\mathbf{K})\exp(i\mathbf{K}\cdot\mathbf{R}),$$

where $\mathbf{K}$ lies in the first Brillouin zone, equation (3.36) is transformed to

$$\sum_{k'=1}^{3}\sum_{l'm'p'}\left(\delta_{kk'}\delta_{ll'}\delta_{mm'}\delta_{pp'}-\frac{1}{s_{k'}}\hat{\Gamma}_{klmp,k'l'm'p'}(\mathbf{K})\right)A_{k'l'm'p'}(\mathbf{K})=z_{klmp}\delta_{\mathbf{k},\mathbf{0}}. \tag{3.37}$$

When $\mathbf{K}\neq 0$, the above equation has only the zero solution, because the eigenvalues of the matrix $\hat{\Gamma}_{klmp,k'l'm'p'}(\mathbf{K})$ lie in the interval $[0,1]$ [6], while $s_{k'}$ cannot be in the same interval. Therefore the determinant of the coefficient matrix cannot be zero. A nonzero solution of the above equation exists only when $\mathbf{K}=0$. As a result, we only need to solve the following equation:

$$\sum_{k'=1}^{3}\sum_{l'm'p'}(\delta_{kk'}\delta_{ll'}\delta_{mm'}\delta_{pp'}-\frac{1}{s_{k'}}\hat{\Gamma}_{klmp,k'l'm'p'})A_{k'l'm'p'}=z_{klmp}, \tag{3.38}$$

where

$$\hat{\Gamma}_{klmp,k'l'm'p'}=\sum_{\mathbf{R}}\hat{\Gamma}_{klmp,k'l'm'p'}(\mathbf{R}). \tag{3.39}$$

When the coefficients A_{klmp} are solved, we immediately obtain

$$A_{klmp}(\mathbf{R})=\sum_{\mathbf{K}}A_{klmp}(\mathbf{K})\exp(i\mathbf{K}\cdot\mathbf{R})=A_{klmp},$$

independent of $\mathbf{R}$ because only the $\mathbf{K}=0$ term is nonzero. The effective dielectric constant can thus be written

$$\overline{\varepsilon}_{zz}=\varepsilon_{\ell}\left(1-\frac{1}{v}\sum_{klmp}\frac{1}{s_k}A_{klmp}z_{klmp}\right), \tag{3.40}$$

where v is the volume of the unit cell.

If the spheres have no coatings, the above formulation can be further simplified. In particular equation (3.38) may be expressed as

$$\sum_{l'm'}(\delta_{ll'}\delta_{mm'} - \frac{1}{s}\hat{\Gamma}_{lm,l'm'})A_{l'm'} = z_{lm}. \tag{3.41}$$

We denote the eigenvalues of the matrix $\hat{\Gamma}_{lm,l'm'}$ as s_u and the corresponding eigenvectors as U_u, with components $U_{u,lm}$. Explicit expressions for the matrix elements of $\hat{\Gamma}$ are given in appendix B for the case of coated spheres. Equation (3.41) can be represented in terms of s_u and $U_{u,lm}$ as

$$A_{lm} = \sum_u \frac{s}{s - s_u} U_{u,lm} \sum_{l'm'} U^*_{u,l'm'} z_{l'm'}. \tag{3.42}$$

The effective dielectric constant can then be written as

$$\begin{aligned}\overline{\varepsilon}_{zz} &= \varepsilon_\ell \left(1 - \sum_u \frac{f_u}{s - s_u}\right) \\ &\equiv \varepsilon_\ell (1 - F(s)),\end{aligned}$$

where

$$F(s) = \sum_u \frac{f_u}{s - s_u} = \sum_u \frac{\frac{1}{v}\left|\sum_{lm} z_{lm} U_{u,lm}\right|^2}{s - s_u} = \sum_u \frac{p\left|U_{u,10}\right|^2}{s - s_u}. \tag{3.43}$$

Here p is the volume fraction of spheres. In the last equality we have used the fact that $z_{lm} = (4\pi a^3/3)^{1/2}\delta_{l1}\delta_{m0}$. Since s_u and f_u depend only on the structure of the system, for systems with different material parameters s and the same structure we need only calculate the structure factors once. For other material systems with the same microgeometry we can simply substitute the material parameters into equation (3.43) to get the effective dielectric constants.

For more complicated systems consisting of several spherical grains in one unit cell, the above formulae can be easily extended. If we denote the relative positions of the grains within one unit cell as $\boldsymbol{\tau}$, then equation (3.38) becomes

$$\sum_{k'=1}^{3} \sum_{l'm'p'\tau'} (\delta_{\tau\tau'}\delta_{kk'}\delta_{ll'}\delta_{mm'}\delta_{pp'} - \frac{1}{s_{k'}}\hat{\Gamma}_{\tau klmp,\tau' k' l' m' p'})A_{\tau' k' l' m' p'} = z_{\tau klmp}, \tag{3.44}$$

and equation (3.41) becomes

$$\overline{\varepsilon}_{zz} = \varepsilon_\ell \left(1 - \frac{1}{v}\sum_{\tau klmp} \frac{1}{s_k} A_{\tau klmp} z_{\tau klmp}\right). \tag{3.45}$$

For spheres with no coatings, we have

$$F(s) = \sum_u \frac{f_u}{s - s_u} = \frac{1}{v}\sum_u \frac{\left|\sum_{\tau lm} z_{\tau lm} U_{u,\tau lm}\right|^2}{s - s_u} = \sum_u \frac{p\sum_\tau \left|U_{u,\tau 10}\right|^2}{s - s_u}. \tag{3.46}$$

For practical calculations the summation in (3.39) has to be evaluated numerically. The summations for $l + l' > 2$ are absolutely convergent while the summation for $l + l' = 2$ is only conditionally convergent. Direct evaluation of the summation in the $l + l' = 2$ case cannot get meaningful results. Summation for small value of $l + l'$ also converges very slowly. For these cases we use the Ewald method for the summations; accurate results can be obtained with only a small computational effort. In our calculations, those with $l + l' \leq 6$ were done with the Ewald

summation method, and the higher order cases by direct summation. Details of the Ewald sums are described in appendix D, where formulae up to $l + l' = 3$ are given.

4. Structure in the DER fluid

A fundamental question of the ER phenomenon is the mesoscopic state (structure on a scale intermediate between the size of the individual spheres and the bulk) of the spheres in the HF limit. Halsey and Toor [28] suggested that the spheres should aggregate to form large columns under an electric field, and the structure within the column is FCC in character; whereas Tao and Sun [5] argued that the structure inside the columns is body-centred tetragonal (BCT). Tao and Sun's argument is based on the self-consistent dipole interaction between polarized spheres; higher order multipoles were ignored. Even though the result of Tao and Sun is physically plausible, the consideration of only the dipole interaction is a serious approximation. Friedberg and Yu [30] have calculated the free energy difference between the BCT and FCC structures by including the quadrupole, octupole and even the 32nd pole. They found that the contributions to the difference of each higher multipole can be either positive or negative. Subsequent studies were carried out based on the exact evaluation of the electrostatic energy by numerical methods such as the finite element method [31–33], the multipole expansion method [34], and the Bergman method [35–37]. These calculations gave consistent results and all concluded that the ground state of the DER fluid is a BCT structure. Martin *et al*. [38] have further simulated the structure formation by thermal coarsening under uniaxial and biaxial fields, and found the Brownian motion to be essential for the formation of equilibrium structures.

In the BCT structure, the chain is the most dominant element. Due to the strong dipolar interaction within a chain they are usually first formed under an applied field. The weak interchain interaction means that the formation of columns from chain–chain aggregation is generally slower and occurs only under a large applied field ($> 500\,\mathrm{V\,mm^{-1}}$). Experimental observation of the mesostructure is more difficult. In an early work, Chen *et al*. [39] concluded from their experiment that the structure of the DER fluid within the columns is BCT, as expected from the theoretical prediction. Later studies by Elliot *et al*. [40], and Dassanayake *et al*. [41] confirmed this conclusion and also gave some insight to the structure and dynamics of the DER fluids. The evolution of chain to column was studied by Wen *et al*. along with the rheological changes [42, 43]. Theoretical and experimental studies of the structure formation have also been done by a number of groups [44–53].

Here, we obtain the ground state of the DER model with spheres (with no coatings) by comparing the free energies of different structures. In the HF limit, $\overline{\varepsilon}_{zz}$ is the volume average of the column dielectric constant, denoted $\overline{\varepsilon}_{zz}^{\mathrm{inf}}$, and the liquid dielectric constant ε_ℓ. Volume averaging is accurate in the present case, due to the anisotropic columnar geometry (the length of the column is much larger than its diameter). Only the surface energy of the columns is neglected, which is shown below to be orders of magnitude smaller. If we denote the solid volume fraction inside the columns as p_{str}, which depends on the given periodic structure, then

$$\overline{\varepsilon}_{zz} = \frac{p}{p_{\mathrm{str}}}\overline{\varepsilon}_{zz}^{\mathrm{inf}} + (1 - \frac{p}{p_{\mathrm{str}}})\varepsilon_\ell. \tag{4.1}$$

The effective dielectric constants of six different structures were calculated, the results are given in tables 1 and 2. The BCT structure has the largest effective dielectric constant, and hence the lowest free energy density. FCC and HCP structures are very close to the BCT structure. In fact, both FCC and HCP have a larger $\bar{\varepsilon}_{zz}^{\inf}$ than that of the BCT structure (table 2). However, $\bar{\varepsilon}_{zz}$ of BCT is larger because it has a smaller p_{str}. So it is the subtle difference in the densities of the different structures which gives BCT the edge as the ground state. This is different from the dipolar case where the BCT structure can be superior even prior to volume averaging.

To account for the surface energy associated with the finite width of columns as observed in the experiments, we have also performed calculations for systems with finite width columns, using the formalisms given by equation (3.41). The structure inside the columns is assumed to be BCT while the columns are arranged in either the hexagonal or the square lattice. In both cases the effective dielectric constants are smaller than that when the column is infinite in size, i.e. less than $\bar{\varepsilon}_{zz}^{\inf}$. We note from figure 1 that the calculated effective dielectric constant scales as $1/\sqrt{N_{\mathrm{c}}}$, where N_{c} denotes the number of chains inside a given column, and tends toward $\bar{\varepsilon}_{zz}^{\inf}$ as N_{c} increases. This scaling demonstrates the fact that the difference between the finite columns and the infinite column arises from the surface energy. This contribution can also be viewed as an attractive interaction between the columns. Since it is

Table 1. The exact effective dielectric constants of several periodic structures, $\bar{\varepsilon}_{zz}$, compared with that in the dipolar approximation. The separation between the spheres is $\delta = 5 \times 10^{-3}$ in terms of the sphere radius, volume fraction of particles is 0.2. Here ε_1 is the dielectric constant of the solid spheres.

		Structure					
$\varepsilon_1/\varepsilon_\ell$		BCT	FCC	HCP	BCC	SC	Diamond
10	Exact	2.167	2.156	2.156	2.043	1.911	1.627
	Dipole	2.031	1.994	1.995	1.905	1.734	1.601
800	Exact	5.173	5.129	5.129	4.205	3.518	1.976
	Dipole	3.376	3.188	3.194	2.798	2.230	1.897

Table 2. The exact effective dielectric constants of several periodic structures, $\bar{\varepsilon}_{zz}^{\inf}$, compared with that in the dipolar approximation. The separation between the spheres is $\delta = 5 \times 10^{-3}$ in terms of the sphere radius. Here ε_1 is the dielectric constant of the solid spheres.

		Structure					
$\varepsilon_1/\varepsilon_\ell$		BCT	FCC	HCP	BCC	SC	Diamond
10	Exact	5.014	5.215	5.216	4.495	3.348	2.050
	Dipole	4.544	4.624	4.629	4.031	2.893	2.006
800	Exact	15.35	16.06	16.06	11.74	7.493	2.634
	Dipole	9.170	8.979	9.003	7.024	4.171	2.503

extremely small, the interaction between the columns is therefore very weak. From figure 1 we estimate the surface energy contribution for a column size of 25 chains to be 3% when $\varepsilon_1/\varepsilon_\ell = 20$. The small magnitude of the surface energy may account for the finite columns seen in most of the ER fluids experiments, as kinetic processes could be dominant.

In the case of coated spheres, the same conclusion can be drawn. That is, the ground state structure of the DER fluid consisting of multiply coated microspheres is still BCT. Figure 2 is a plot of the effective dielectric constant of coated spheres as a function of the core sphere dielectric constant for different structures. Figure 3 is a plot of effective dielectric constant of coated spheres as a function of the first coated layer dielectric constant for different structures. We see that BCT has the largest effective dielectric constant and FCC is always a close second.

We also performed $\epsilon_{zz}^{\inf}$ calculations with different structures where the unit cell size is larger than the sphere diameter, so that the spheres are separated. The results are displayed in figures 4 and 5. It is seen that the touching sphere case has the largest $\overline{\varepsilon}_{zz}^{\inf}$. Here the interesting observation is that the variation of $\overline{\varepsilon}_{zz}^{\inf}$ is linear in the vicinity of the close packing density. That implies an inward electrostatic pressure on each sphere. Thus any separation between neighbouring spheres implies higher energy.

We conclude from our first-principle calculations that the HF ground state of the DER fluids is the BCT structure formed by microspheres. This result, while not a mathematical proof, is supported by experimental evidence (see below). The finite column size observed in DER fluids may be the result of hydrodynamic interaction and kinetic processes. It is not determined by the minimum of the Gibbs free energy. It is conjectured that the thermodynamic ground state cannot be realized in experiments because the interaction between the columns is weak, so that the columns are pinned at positions where they are formed.

It should be noted that the ground state structure of conducting spheres, or particles with high surface conductivity, can be drastically different from the BCT columns as described above. This is because the conducting particles would effectively modify the electrodes, with significant electric field enhancement at the tips of the resulting structures, thereby increasing the probability of sphere attachment at these points. That is, the tips of the conducting structure define the

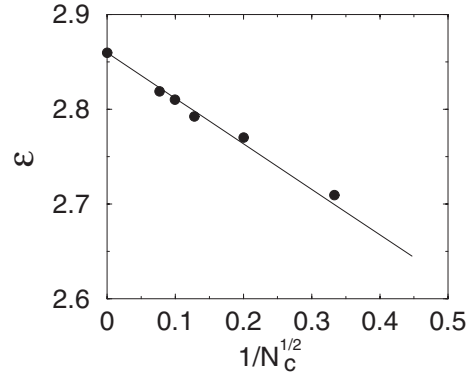

Figure 1. The calculated effective dielectric constant plotted as a function of the inverse column size for different structures. Here $\varepsilon_1/\varepsilon_\ell = 20$, $p = 0.2$, $\varepsilon_\ell = 1$. The inverse $\sqrt{N_c}$ dependence means that the slope is indicative of the surface energy.

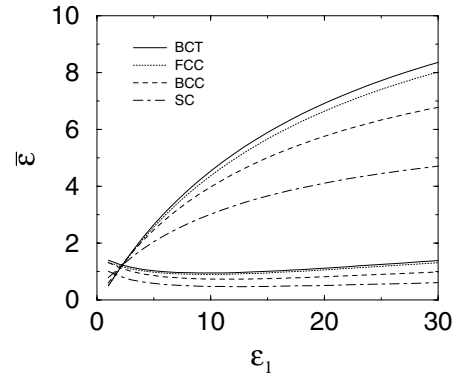

Figure 2. The effective dielectric constant of doubly coated spheres as function of inner sphere dielectric constant, where the radius of the inner sphere is 0.9 in units of the sphere radius, and the thickness of the first coated layer is 0.09, with a dielectric constant of $-5+10$i. The thickness of outer coated layer is 0.01 with a dielectric constant 2, and the fluid dielectric constant is 1. Upper curves are real part and lower curves are imaginary part of the effective dielectric constant. The volume fraction is 0.2.

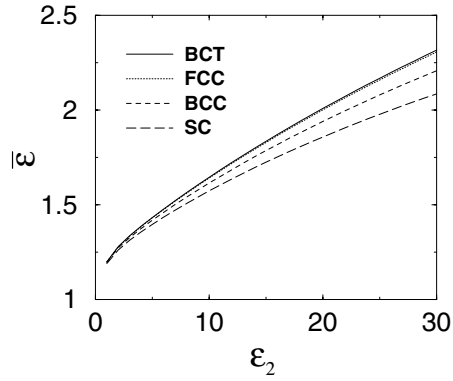

Figure 3. The effective dielectric constant of doubly coated spheres as a function of the inner coating dielectric constant, where the radius of the inner sphere is 0.9 in units of the sphere radius, with a dielectric constant 2, and the thickness of the inner coating is 0.09. The thickness of the outer coating is 0.01 with a dielectric constant 2, and the fluid dielectric constant is 1. The volume fraction is 0.2.

dynamic growth points. Thus it is not surprising that the observed ground state has a fractal structure resembling that of the diffusion-limited aggregates (DLA) [54, 55], also shown below.

5. Static yield stress of the DER fluid

The yield stress can be calculated by delineating a shear distortion and then calculating the free energy difference between the sheared system and the ground state. By shearing the system perpendicular to the applied electric field, the columns originally along the applied field will tilt away from the field direction, thus lengthening the chains inside each column. This necessitates spacings between the neighbouring spheres within a chain, as well as spacings between neighbouring

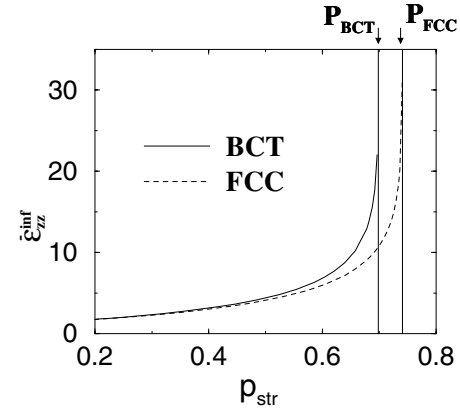

Figure 4. $\bar{\varepsilon}_{zz}^{\inf}$ plotted as a function of packing fraction for BCT and FCC. The maximum value of $p_{\mathrm{BCT}} = 2\pi/9 = 0.69813\ldots$ and $p_{\mathrm{FCC}} = \pi/3\sqrt{2} = p.74048\ldots$.

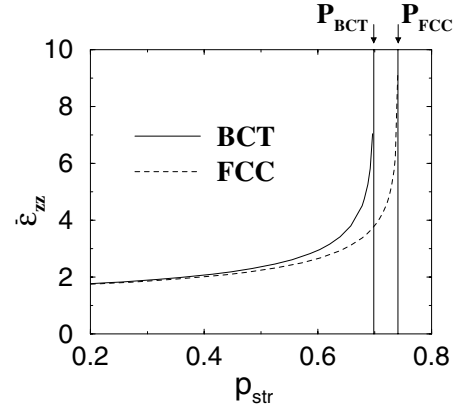

Figure 5. $\bar{\varepsilon}_{zz}$ plotted as a function of packing fraction for the BCT and FCC arrangements of spheres. Here the concentration of solid spheres is $p = 0.2$. It should be noted that the derivative of the curve at maximum BCT packing fraction is not zero. Therefore there is an inward electrostatic pressure on each sphere, exerted by the neighbouring spheres.

chains. While the intra-chain spacings are maintained by the shearing force, the inter-chain spacings are unstable since decreasing such spacings would lower the energy. Thus the lowest-energy shear distortion path is shown in figure 6: a lengthening of the chains is accompanied by a shrinking of the chain–chain separation, so as to maintain contact between neighbouring chains. Such a shear distortion is characterized by an angle θ, and involves a change in unit cell volume given by

$$\frac{v}{v_0} = \frac{4\cos^2\theta - 1}{3\cos^3\theta}, \tag{5.1}$$

where v_0 is the cell volume at $\theta = 0$.

There are many literature references dealing with the calculation of yield stress by different approaches; Wu and Conrad have developed several models based on

different approximations [56–58]. Theories based on the finite element method [32] and multipole expansion method [59, 60] have also been developed. The starting point of the work by Clercx and Bossis [59] is the same as ours [35], by expanding the electrostatic field in vector spherical harmonic functions. They succeeded in obtaining an exact representation of the electrostatic energy as a function of structure and component dielectric constants. The yield stress and shear modulus were evaluated by differentiation. This method gives the exact value of the static yield stress, just as in our case. There are other approximate theories of yield stress [61–64]. In a recent publication, Choi *et al.* [65] gave a scaling function for the yield stress. Below we describe the yield stress and shear modulus calculation within our approach.

When the system is sheared, the columns cannot remain aligned in the direction of the applied field. Let z' be the column direction in the sheared system, and x' be the direction perpendicular to z' in the plane determined by the field direction and the column direction. In the tilted coordinate frame, the structure is uniaxial with z' as the axis of symmetry. In that frame, there can be a finite $\overline{\varepsilon}_{z'x'}$ (or $\overline{\varepsilon}_{x'z'}$) due to surface fields. However, these are negligibly small as shown before. Thus only $\overline{\varepsilon}_{z'z'}$ and $\overline{\varepsilon}_{x'x'}$ matter. By using the structure particular to a sheared column at angle θ as described above and in figure 6, the $z'z'$ component of the effective dielectric constant tensor can be evaluated by first calculating the infinite column effective dielectric constant along the $z'z'$ direction, and then performing a volume average. The component $\overline{\varepsilon}_{x'x'}$ can be evaluated by first calculating the infinite column dielectric constant in the $x'x'$ direction, $\overline{\varepsilon}^{\inf}_{x'x'}$, and then obtaining $\overline{\varepsilon}_{x'x'}$ by the Maxwell–Garnett formula [66, 67]

$$\frac{\overline{\varepsilon}_{x'x'}-1}{\overline{\varepsilon}_{x'x'}+1}=\frac{p}{p_{\mathrm{str}}}\frac{\overline{\varepsilon}^{\inf}_{x'x'}-1}{\overline{\varepsilon}^{\inf}_{x'x'}+1}. \tag{5.2}$$

This approximation is justified by the following two facts. First, the contribution due to $\overline{\varepsilon}_{x'x'}$ is small when θ is small. Second, the Maxwell–Garnett formula becomes accurate when the separation between the columns tends to infinity, and here the

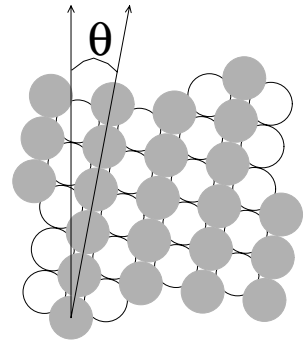

Figure 6. Definition of the shear distortion used in the calculation of the shear modulus and yield stress. Two layers of the sheared structure are shown. The dark solid circles denote the top layer; the open circles denote the lower layer. Angle θ is relative to the c axis of the un-sheared state. Shearing distortion slightly elongates the c axis, accompanied by an inward shrinkage of the a axis so as to maintain contact between the neighbouring chains.

columns are well separated because p/p_{str} is less than 0.3 in most cases. $\overline{\varepsilon}_{zz}$ is simply related to $\overline{\varepsilon}_{z'z'}$ and $\overline{\varepsilon}_{x'x'}$ by the formula

$$\overline{\varepsilon}_{zz} = \overline{\varepsilon}_{z'z'} \cos^2\theta + \overline{\varepsilon}_{x'x'} \sin^2\theta \tag{5.3}$$

through the rotational transformation of a second rank tensor.

By varying θ, we have numerically calculated the free energy density as a function of strain; the stress is obtained simply by differentiation. A typical stress–strain relation, shown in figure 7, is noted to start at zero and is linear at small strain. It reaches a maximum and decreases with strain when sheared further. The initial slope gives the shear modulus, and the maximum of the stress–strain relation is defined as the static yield stress. The part after the maximum is plotted as a dashed line, since decreasing stress with increasing strain indicates instability.

6. Upper bounds of the yield stress and shear modulus

One important question concerning ER fluid application is the yield stress upper bound. Both physically and mathematically, the yield stress is known to increase with the ratio between the particle and the fluid dielectric constants. The upper bound may be obtained by setting that ratio to infinity, i.e. $s \to 0$. However, as the value of $s \to 0$, the question of whether the spheres are actually touching becomes crucial. For the purpose of constructing a physical upper bound, we assume that (1) $|\varepsilon_1/\varepsilon_\ell| \to \infty$, (2) the surfaces of the spheres cannot approach each other closer than a small distance 2δ, e.g. the lower limit on atomic separation (so the lowest s_n is slightly greater than 0), and (3) $p \le p_{\mathrm{BCT}} = 2\pi/9$. Figure 8 is the calculated effective dielectric constant under the above mentioned conditions as a function of δ/R. The solid line is $\overline{\varepsilon}_{zz}/\varepsilon_\ell = -3.95\ln(\delta/R) - 5.35$. We see that at small δ/R the extrapolation is very good. The calculated upper bounds of static yield stress and shear modulus are shown in figures 9 and 10, plotted as functions of δ/R. In units of $|\varepsilon_\ell|E^2/8\pi$, the fitted solid line is $1.38\sqrt{R/\delta}$ for the static yield stress, and $1.9(R/\delta)$ for the shear modulus. Taking $R = 20\,\mu\mathrm{m}$, $\delta = 1\,\text{Å}$, $E = 1\ \mathrm{kV\,mm^{-1}}$, and $\varepsilon_\ell = 2.5$, we get 8 kPa and 4 MPa, respectively, for the two bounds. Since these upper bounds are obtained

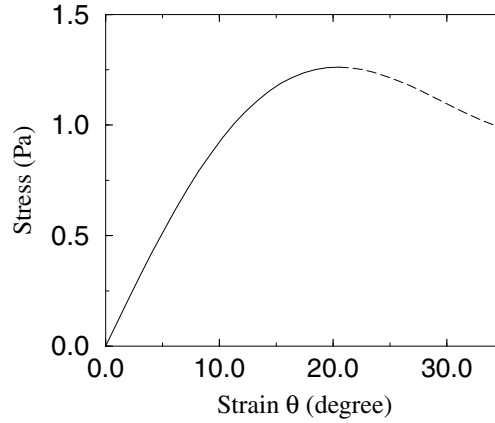

Figure 7. Stress calculated as a function of strain. Here the linear region (small θ) defines the shear modulus. The maximum defines the (static) yield stress. The dashed line indicates the unstable regime. The curve is calculated with $\varepsilon_\ell = 2.71$, $\varepsilon_1 = 8.4 + 0.43\mathrm{i}$, $E = 1.32\,\mathrm{kV\,mm^{-1}}$, and $p = 0.22$.

by setting $s \to 0$, they are independent of whether we use complex or real ε_1 and ε_ℓ. The square root dependence of the yield stress with the sphere separations can be understood physically by the following argument. Consider two conducting spheres of radius R in close proximity to each other, with a separation δ between their surfaces at the point of closest approach. Provided $R \gg \delta$, the mutual capacitance has the form

$$C \propto \ln \frac{R}{\delta}.$$

Under an applied electric field E along the axis joining the centres of the two spheres, the leading order term of the free energy density is proportional to C. If now we apply a shear perpendicular to the electric field, the line segment joining the centres of the two spheres will be both tilted with an angle θ with respect to the electric field

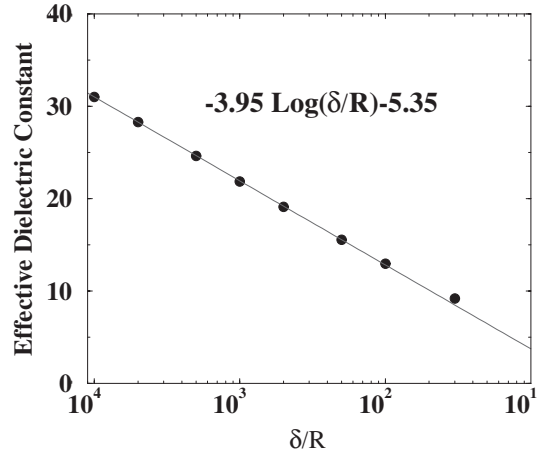

Figure 8. Calculated effective dielctric constant in the limit of $|\varepsilon_1/\varepsilon_\ell| \to \infty$, plotted as function of δ/R. The solid line is the best fit.

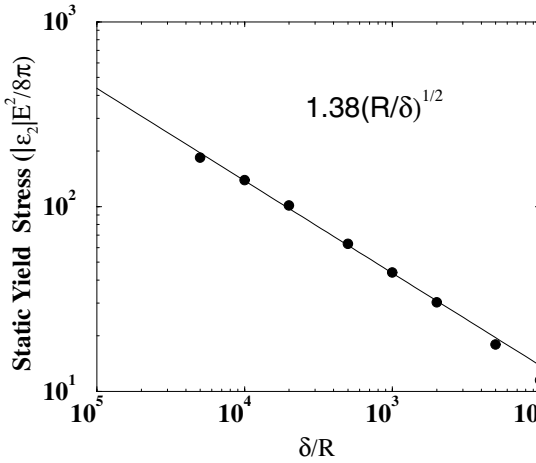

Figure 9. Calculated upper bound of the (static) yield stress as function of δ/R (symbols). The solid line is the best fit.

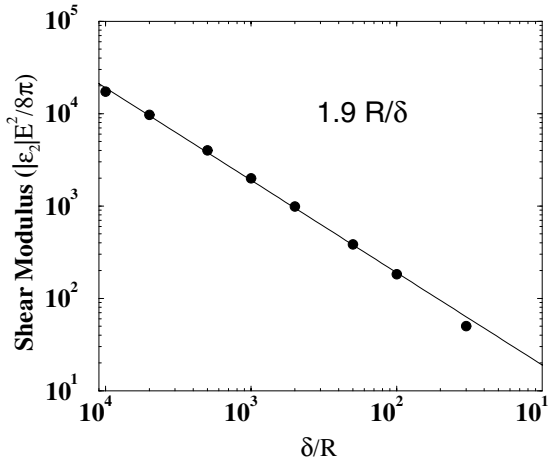

Figure 10. Calculated upper bound of the shear modulus as function of δ/R (symbols). Solid line is the best fit.

direction, as well as lengthened. If the new separation is denoted d, then $(2R + d)\cos\theta = 2R + \delta$, so that $d \approx \delta + R\theta^2$ for small θ. Within the small angle approximation, the shear stress is proportional to $-(\partial C/\partial\theta) \propto (R/d)[(d - \delta)/R]^{1/2}$, which is noted to have a peak value. The static yield stress is defined by the peak value of the shear stress, given by the condition $d = 2\delta$, so that the static yield stress $\propto (R/d)^{1/2}(\varepsilon_\ell E^2/8\pi)$, where the quantity in the parentheses is the unit of energy density in the present problem.

In arriving at the above bounds no consideration has been given to dielectric breakdown, which would limit the actual systems from achieving the bounding values. Surface roughness of the particles is also not considered, as it is not relevant to the electrostatic part of the system energy.

The yield stress upper bound and the associated heuristic argument suggest the following coated sphere structure for optimizing the yield stress and other application characteristics of the DER fluid. The solid particle should have a low density dielectric core so as best to match the density of the liquid and prevent sedimentation. A thin metallic coating can give the particle large polarizability and hence dielectric constant. An additional insulating coating thickness should be optimized so that it prevents electrical shorting between the conducting spheres and provides wear resistance on the one hand, and gives a large yield stress on the other. In this regard, a large dielectric constant for the coating material (or the liquid) is a plus, as it increases the capacitance between the spheres. Since the yield stress depends on the ratio between R and δ, a large R/δ is favoured.

7. Comparison with experiments

The ER fluids of our experiments consist of uniform sized 1.5 μm glass spheres (Nippon Shokubai, product KE-P150) suspended in silicone oil. To prepare the samples, both glass spheres and oil were heated at a temperature of 100–120°C for at least 5 h to remove traces of water.

For measurement of the dielectric constant, an ER fluid cell was made with two brass plates serving as the electrodes, separated by a plastic frame. The dimension of

the cell was $30 \times 30 \times 2\,\text{mm}^3$, with a 2 mm gap between the electrodes. The dielectric measurement of ER fluids as a function of frequency was performed by using a HP4284A LCR meter in the frequency range 20 Hz to 100 kHz.

The static yield stress was measured by using a standard parallel plate torsional device with a root-mean-square (rms) electric field applied across the ER fluids, sandwiched between the parallel plates. The lower plate was rotated slowly, dragging the top plate which was connected to a torque meter. The static yield stress was read when relative slipping occurred between the two plates. The power supply used in our experiments was specially designed with a sinusoidal voltage output and tunable frequency ranging from 30 to 8 000 Hz. Because of the effect of transformer inductance, the output voltage was monitored *in situ* to keep it stable over the whole measuring frequency range.

We give here the experimental measurements on the ground state mesostructure of the HF DER fluid, the yield stress of the DER fluid, and the structure-induced dielectric nonlinearity. Comparisons with our theoretical predictions are also presented.

7.1. *Mesostructure of the DER fluid*

We have confirmed our theoretical prediction experimentally that BCT is the favoured structure inside the ER fluid columns, in the HF regime. Figure 11 shows the process of column formation as the field strength is increased. We observed that the spheres were initially randomly dispersed in the absence of an applied field, figure 11(*a*). As the electric field was increased in strength, chains formed along the field direction, then coalesced and coarsened to form columns, see figures 11 (*b–d*). In order to observe the structure inside the column, epoxy was employed as the liquid matrix instead of silicone oil. Cross-sectional SEM micrographs were obtained by freezing (solidifying) the columns inside the epoxy and then cutting them layer by layer. Figures 11 (*e, f*) are for configuration at fixed $E = 2\,\text{kV mm}^{-1}$, cut along the (0 0 1) and (1 1 0) planes. It is seen that the cut along the (0 0 1) plane displays a central sphere surrounded by four spheres shifted out of the cutting plane. The (1 1 0) plane displays a hexagonal lattice. Taken together, they give direct evidence for the BCT structure.

In the right panels of figure 12 we present the observed mesostructure of the ER fluid with conducting microspheres (50 μm diameter glass spheres coated with a 1 μm thick layer of nickel), and contrast them with the mesostructures of the DER fluid with insulating microspheres (left panels). Three different electrode configurations were used. It is clear that the mesostructures of the conducting cases differ significantly from that for the insulating cases, for the reason explained in section 4.

7.2. *The yield stress of dry glass–oil DER fluids*

In figure 13, we compare the measured frequency-dependent static yield stress values of the dried ER sample (solid symbols) with those predicted theoretically (solid lines). In curve A, the high frequency value of the yield stress was calculated with no adjustable parameters. The parameters $\varepsilon_1 = \varepsilon_\infty = 7.8$, $\varepsilon_\ell = 2.71$ used in the calculation were measured independently. The agreement with experiment is seen to be excellent. To explain the slight frequency dependence, we have used the value of $\tau = 4.8 \times 10^{-4}$ s and $\varepsilon_\Delta = 2$ in the Debye form of the glass dielectric constant

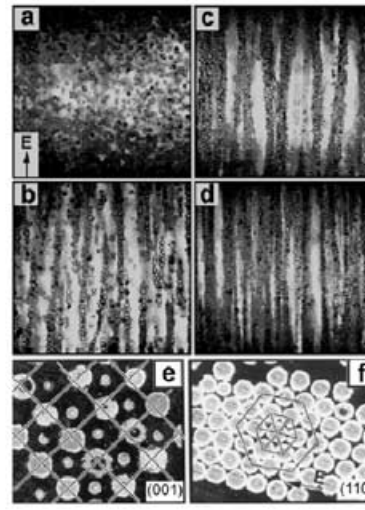

Figure 11. The process of column formation under an increasing electric field, (*a*) to (*d*). The applied field is $E = 0$ in (*a*), $E = 500\,\mathrm{V\,mm^{-1}}$ in (*b*), $E = 900\,\mathrm{V\,mm^{-1}}$ in (*c*), and $E = 1200\,\mathrm{V\,mm^{-1}}$ in (*d*). (*e*) and (*f*) are scanning electron microscope pictures of the particle mesostructure inside a column, obtained by freezing the structure in epoxy and sectioning the resulting sample. (*e*) gives the (0 0 1) cross-section, (*f*) gives the (0 1 1) cross-section. Together they uniquely determine the structure to be BCT. Other than in those cases explicitly stated as having trace water, all silica spheres were dried prior to the experiments.

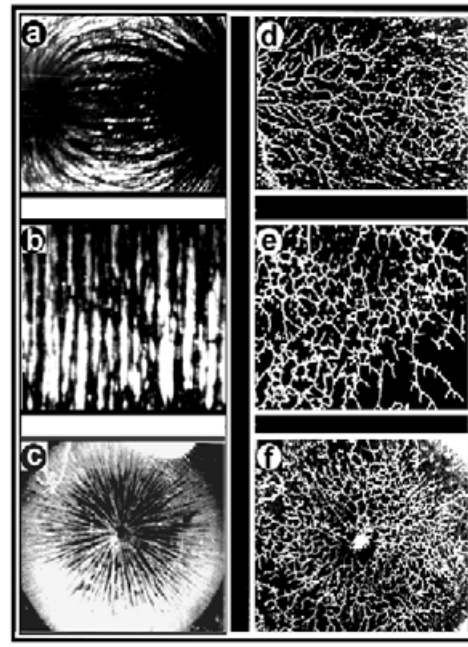

Figure 12. Electric field-induced two-dimensional patterns formed by insulating (*a–c*) (left panels) and conducting (*d–f*) (right panels) particles. Here (*a*) and (*d*) correspond to needle-shaped electrodes pointing towards each other, (*b*) and (*e*) correspond to parallel plate electrodes, and (*c*) and (*f*) correspond to the cylindrically symmetric electrode configuration [78].

$$\varepsilon = \varepsilon_\infty + \frac{\varepsilon_\Delta}{1 - i\omega\tau}. \tag{7.1}$$

Curve B gives the yield stress for the same ER system prior to water removal (i.e. baking at elevated temperatures). It is seen that both the value of yield stress and its frequency dependence are much larger. The theoretical curve is calculated by using

$$\varepsilon_{\text{glass}} = 14.8 + \frac{12}{1 - i\omega\tau}, \tag{7.2}$$

with $\tau = 6 \times 10^{-4}$ s and the measured $\varepsilon_\ell = 2.71$. A plausible explanation for the significant effect of trace water is that under a high electric field the water is attracted to the interface between oil and glass, coating the glass particles and thus modifying its effective dielectric constant. As silica surfaces are known to have a negative zeta potential in the order of -90 meV [68], a reasonable explanation of the relaxation dynamics could be the dynamic re-adjustment of the Debye double layer (present with trace water under the action of the zeta potential) that results under the high interparticle electric field. By using the same parameters and the high field BCT structure, the calculated conductivity of the system at 10 kHz is 2.5×10^{-8} S m^{-1}. This compares favourably with the measured value of 3×10^{-8} S m^{-1} at the same frequency.

Our results thus demonstrate that the observed frequency dependence of the ER fluids yield stress can be traced to the Debye relaxation processes common in poor insulators, and may be explained quantitatively by the DER model.

The frequency dependence of the shear modulus for the same systems can also be directly evaluated. Here, unfortunately, no experimental data are yet available. The calculated results (solid lines), using the same parameters as those in figure 13, show similarity to that of the yield stress. However, when ε_Δ is large, a novel phenomenon is predicted. That is, over some finite frequency range it is found that the ground state is unstable to a slight elongational distortion of the BCT lattice, and the new ground state is one where the c axis is elongated and the a axis correspondingly shortened. The dashed line in figure 14 is calculated by using $\varepsilon_\ell = 2.71$,

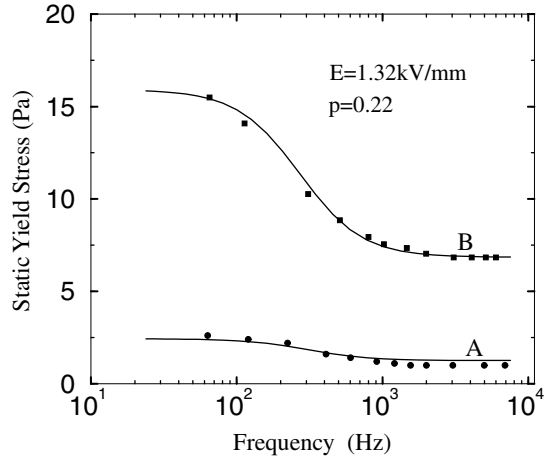

Figure 13. The calculated (solid line) and measured (symbols) static yield stress of two DER fluids. A is for a dried sample where water has been removed. B is for an as-prepared sample where there may be a trace amount of water.

$\varepsilon_1 = 14.8 + \frac{85}{1-i\omega\tau}$, with $\tau = 6 \times 10^{-4}$ s. It indicates two frequencies where there are soft modes associated with the structural instability (shear modulus is zero). Between these two frequencies the ground state is still a BCT structure, but with the c axis elongated by up to 0.85%, and the a axis shortened. The shear modulus for those frequencies intermediate between the two soft mode frequencies is calculated with respect to the alternative ground state. It is interesting to note that in contrast to the shear modulus, the yield stress calculated with the same parameters gives no hint of any irregularities at finite frequencies. The reason may be gathered from figure 7, which indicates that the yield stress is always defined at finite values of θ, and the difference between the two ground states is negligible at those tilt angles.

We have also measured the dielectric constant and static yield stress on samples with predetermined amounts of water, and fitted the data by assuming the dielectric constants of both the watered oil and glass spheres to be of the Debye form with a distribution of relaxation times. The experimental results can be well explained by the theory [36]. In particular, once the effective dielectric constants (real and imaginary parts) of the samples are fitted, the yield stress data can be reasonably well explained with no adjustable parameters. These results rule out the 'water bridge' mechanism [69] (where the water trapped in the contact areas between particles is held responsible for holding the particles together) as a significant contributor to the yield stress in our system. It should be noted that the Debye model also includes, as a special case, the model developed by Anderson [70], based on the limit of a large imaginary part of the dielectric constant, i.e. when the conductivity of the solid spheres dominates.

7.3. *Structure-induced dielectric nonlinearity*

In this experiment, a unique material—denoted as electro-magneto (EM) microspheres—was used to investigate the anisotropic dielectric properties of ER fluids. The EM microsphere was made of a glassy core onto which a magnetic layer and a dielectric layer were sequentially coated. Since the inner layer is ferromagnetic, the

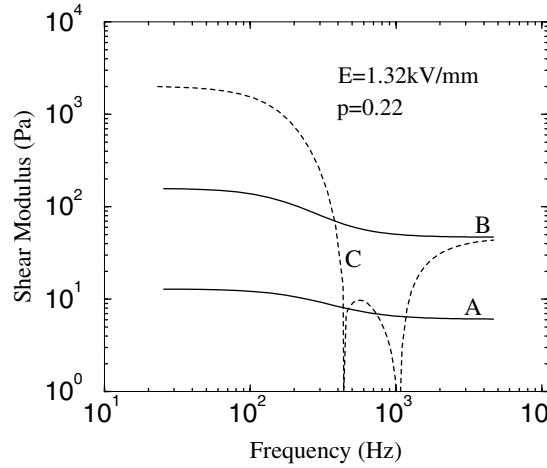

Figure 14. Calculated shear modulus of the DER fluids. Here A and B are for the two samples shown in figure 13; C is for a case calculated with parameters given in the text. Structural instability at two frequencies is indicated.

application of an external magnetic field led to the aggregation of spheres into columns aligned in the field direction, with a BCT arrangement of spheres inside the columns [71]. The structure-induced dielectric variation can thus be determined electrically. The microspheres used here are uniform in size so that the results may be compared directly with theoretical predictions.

The particles used in this experiment consist of $35 \pm 3\,\mu m$ diameter glass spheres onto which an inner magnetic nickel layer and an outer dielectric layer, such as lead zirconate titanate (PZT) or TiO_2, were coated by using electroless plating and sol–gel processes [72, 73]. The magnetization of each individual microsphere, μ_i, can be controlled by adjusting the thickness of the nickel layer. In our experiment, the average thickness of the nickel layer was $2.5 \pm 0.3\,\mu m$; the magnetization of one such sphere was estimated to be $\sim 30\,emu\,g^{-1}$. It should be emphasized here that the thickness of the nickel layer should be at least $2\,\mu m$, otherwise the magnetization of each spheres is too small for suspension in the fluid, even in a relatively strong field. To obtain a strong insulating outer layer, at least five repeat dielectric coatings were made. The prepared particles were annealed at 500°C for 2 h. The cross-sectional SEM image of a well coated microsphere is shown in the upper inset of figure 15, where the inner Ni magnetic layer and the outer PZT insulating layer are clearly visible. The process for TiO_2 coating is the same as for the PZT case.

Figure 15 gives a schematic picture of the experimental set-up for the dielectric measurement. In essence, the sample was placed between the poles of an electromagnet so that the particles were aggregated to form chains and columns aligned along the magnetic field. The dielectric constant parallel and perpendicular to the anisotropy direction can be measured as a function of the applied magnetic field. Here the magnetic field was used to simulate the effect of the electric field on the microgeometry. The observed dielectric constant variation as a function of the applied magnetic field may be interpreted as a nonlinear effect. Figure 16 (*a*) shows the randomly dispersed particles in silicone oil at zero magnetic field. As the field strength was increased the particles began to align to form chains in the field direction. With further field increase the chains coarsened to form columns across the two poles. The coarsening process is shown in figures 16 (*b*, *c*).

Figures 17 (*a*) and 17 (*b*) show, corresponding to the structure changes, the measured variations of real (ε') and imaginary (ε'') parts of the dielectric constant as a function of applied magnetic field strength for two samples. In the figures, *zz*(*xx*) indicates the test configuration where the two electrodes of the ER fluid cell were placed parallel (perpendicular) to the magnetic field direction. For the *zz* case, it is seen that both the real and imaginary parts of the dielectric constant increased monotonically as the magnetic field strength was increased from 0 to 2 500 G; beyond that, there was only a slight increase. The increase in the real parts of the dielectric constant for the PZT- and TiO_2-coated ER fluids is 7% and 4%, respectively, and the imaginary parts for both cases are increased by 7%. For the *xx* case, however, both the real and imaginary parts decreased as the magnetic field strength was increased. It should be remarked that from visual microscope observations, beyond 150 G no visible change in the column structure can be identified. We believe that the slight increase in the dielectric constant at high magnetic field is due to small adjustments among the particles.

To explain the experimental results described above, we used the following calculations to obtain the *zz* and *xx* components of the effect dielectric tensor. Since the ER system before the formation of the columns is a random dispersion of

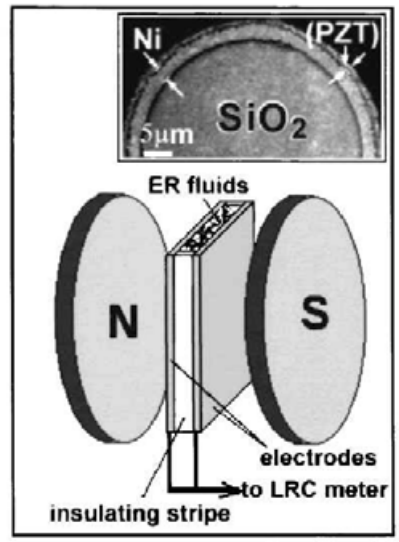

Figure 15. Schematic diagram of the measurement set-up. The upper inset shows the cross-sectional SEM imaging of a doubly coated microsphere.

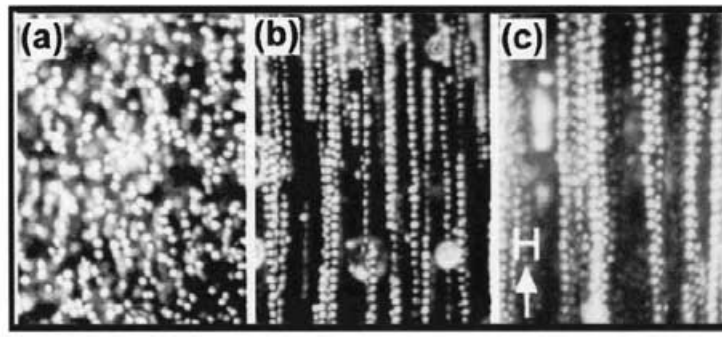

Figure 16. Structure evolution as the magnetic field strength is increased. Here the field strengths for (*a*), (*b*) and (*c*) are 0, 30 and 200 G, respectively.

particles, its effective complex dielectric constant can be calculated by the Maxwell–Garnett formula,

$$\frac{\overline{\varepsilon}-\varepsilon_\ell}{\overline{\varepsilon}+2\varepsilon_\ell}=p\frac{\varepsilon_p-\varepsilon_\ell}{\varepsilon_p+2\varepsilon_\ell}. \tag{7.3}$$

Here the subscripts p, ℓ stand for particle and liquid, respectively; $\overline{\varepsilon}$ is the effective dielectric constant, and p is the volume fraction of solid particles. From the measured effective dielectric constant (with the frequency of the LCR meter fixed at 1 kHz) of the mixture and the dielectric constant of the oil (2.71), one can deduce from the above formula the dielectric constant of the solid particle, ε_1. This information, together with the known ε_ℓ, enables us to calculate s, which constitutes the input to the high field dielectric constant calculations. Under a high field, since the particles form columns along the z direction, the zz component of the effective dielectric constant is given by equation (4.1). Considering the slight dispersion in the sphere size in this experiment, we made a calculation with uniform sized spheres but

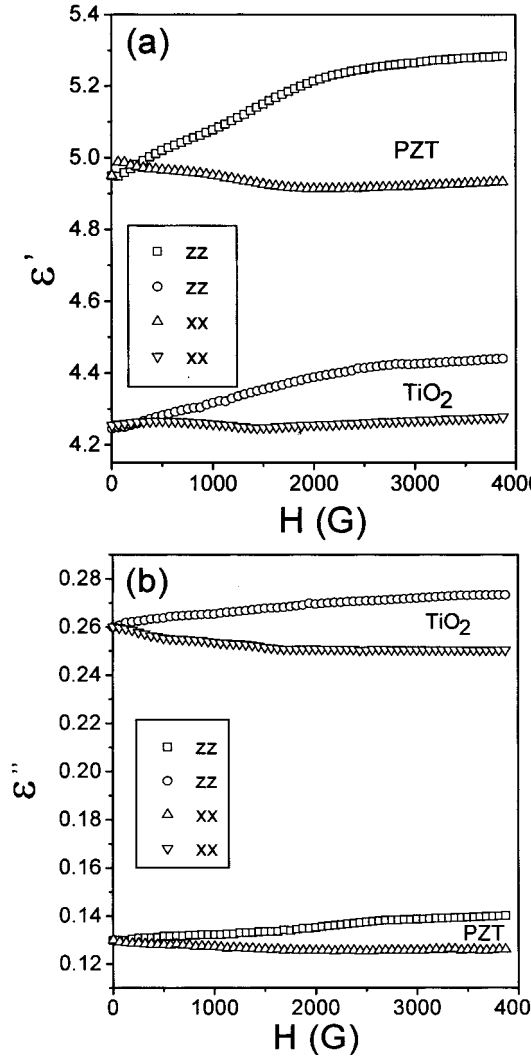

Figure 17. Dependences of real (*a*) and imaginary (*b*) parts of the dielectric constant on applied magnetic field strength. Here the volume fraction is 0.27, and the frequency of the LCR meter is fixed at 1kHz.

kept them slightly separated, the separation between spheres being 0.15 (here 0.15 is chosen to fit our experimental results in the whole fitting process) times the sphere diameter. The calculated results can be represented accurately by the formula

$$\overline{\varepsilon}_{zz}^{\inf} = \varepsilon_\ell \left(1 - \frac{0.4509}{s - 0.1613} - \frac{0.0058}{s - 0.4187} - \frac{0.0006}{s - 0.4481} - \frac{0.0018}{s - 0.4959}\right), \tag{7.4}$$

which is a truncated form of the Bergman–Milton representation. The *xx* component of the effective dielectric constant can be calculated by the two-dimensional Maxwell–Garnett formula

Table 3. Experimental and theoretical results of the real and imaginary parts of ER fluid dielectric constants measured along the z and x directions for the random and structured cases.

Structure		Theory		Experiment	
		ε'	ε''	ε'	ε''
Random		Fitted	Fitted	4.95	0.13
PZT-column	zz	5.67	0.23	5.29	0.14
	xx	4.75	0.11	4.94	0.12
Random		Fitted	Fitted	4.26	0.26
PZT-column	zz	4.56	0.37	4.44	0.28
	xx	4.15	0.23	4.25	0.25

$$\frac{\overline{\varepsilon}_{xx} - \varepsilon_\ell}{\overline{\varepsilon}_{xx} + \varepsilon_\ell} = \frac{p}{p_{\mathrm{str}}} \frac{\overline{\varepsilon}_{xx}^{\mathrm{inf}} - \varepsilon_\ell}{\overline{\varepsilon}_{xx}^{\mathrm{inf}} + \varepsilon_\ell}, \tag{7.5}$$

where $\overline{\varepsilon}_{xx}^{\mathrm{inf}}$ is approximated by

$$\overline{\varepsilon}_{xx}^{\mathrm{inf}} = \varepsilon_\ell \left(1 - \frac{0.4351}{s - 0.1741} - \frac{0.0157}{s - 0.3944} - \frac{0.0019}{s - 0.4451} - \frac{0.0050}{s - 0.4972} - \frac{0.0013}{s - 0.5456} \right). \tag{7.6}$$

In table 3 we give a comparison of measured and calculated results. The agreement is satisfactory considering the idealized model used in our calculations. However, the observed increase in $\overline{\varepsilon}_{zz}$ is invariably smaller than the theoretical prediction; this could be due to imperfections in the crystalline BCT structure.

8. Summary and discussion

In this article we have given a detailed presentation of a first principles theory of DER fluids based on the Bergman–Milton representation of the effective dielectric constant. The theory treats the dielectric and conductivity effects within a consistent and unified framework, where effects such as the local fields and multiple interactions are treated exactly. With only the dielectric constants of fluid and solid constituents as inputs, predictions of the structure of the high field crystal, with its associated static yield stress and shear modulus, can be calculated with no adjustable parameters. We present extensive experimental results on the structure, yield stress, and dielectric nonlinearity of the DER fluids, and comparison with the relevant theoretical predictions. The excellent agreement obtained shows the static properties of the DER fluids to be accountable by electrostatics.

There are, however, aspects of the DER fluids that still remain to be understood more fully. The size of the columns in the high field state is one such problem. The dynamics of the DER fluids, incorporating both hydrodynamic and electrostatic interactions, is another. While attempts at such dynamic theories have been made in past decades, complete success still seems lacking at present.

Acknowledgements

This work was supported by HKUST-RI 93/94.SC09, CERG HKUST-6142/97P, 6136/97P, 6152/00P, NSFC10029401 and the William Wong Solid State Cluster

Laboratory. H. Ma was also supported by the National Natural Science Foundation of China.

Appendix A. Basis functions

In this appendix we calculate the eigenvalues and eigenfunctions of sphere and spherical shell. From the definition, equation (3.24)

$$\hat{\Gamma}_i\phi(\mathbf{r}) \equiv \int \mathrm{d}V'\eta_i(\mathbf{r}')\nabla'G(\mathbf{r},\mathbf{r}')\cdot\nabla'\phi(\mathbf{r}'). \tag{A 1}$$

Integration by parts of the right hand side gives

$$\int \mathrm{d}V'\eta_i(\mathbf{r}')\nabla'G(\mathbf{r},\mathbf{r}')\cdot\nabla\phi(\mathbf{r}') = \int d\mathbf{S}'\cdot\nabla'G(\mathbf{r},\mathbf{r}')\phi(\mathbf{r}') + \phi(\mathbf{r})\eta_i(\mathbf{r}). \tag{A 2}$$

The integration on the right hand side of (A 2) is on the outer surface of the grain. The eigenvalue equation can therefore be written alternatively as

$$\int \mathrm{d}\mathbf{S}'\cdot\nabla'G(\mathbf{r},\mathbf{r}')\phi_u(\mathbf{r}') + \phi_u(\mathbf{r})\eta_i(\mathbf{r}) = s_u\phi_u(\mathbf{r}). \tag{A 3}$$

A.1. *Spherical particles*

For spherical particles of radius a, by taking the origin to be the centre of the sphere, the expression (A 3) simplifies to

$$a^2\int \mathrm{d}\Omega'\frac{\partial}{\partial r'}G(\mathbf{r},\mathbf{r}')|_{r'=a} + \phi_u(\mathbf{r})\eta_i(\mathbf{r}) = s_u\phi_u(\mathbf{r}). \tag{A 4}$$

The Green's function in the infinite volume limit can be written as

$$G(\mathbf{r},\mathbf{r}') = \frac{1}{4\pi|\mathbf{r}-\mathbf{r}'|} = \sum_{lm}\frac{1}{2l+1}\frac{r_<^l}{r_>^{l+1}}Y_{lm}(\theta,\phi)Y_{lm}^*(\theta',\phi'), \tag{A 5}$$

where $r_< = \min(r,r')$ and $r_> = \max(r,r')$. To solve equation (A 3), we first expand $\phi(r,\theta,\phi)$ in terms of the spherical harmonics as

$$\phi(r,\theta,\phi) = \sum_{lm} f_l(r)Y_{lm}(\theta,\phi), \tag{A 6}$$

and then substitute it into (A 3). From equation (A 4) we get

$$a^2\sum_{lm}\begin{bmatrix}\dfrac{l}{2l+1}\dfrac{a^{l-1}}{r^{l+1}}\\ -\dfrac{l+1}{2l+1}\dfrac{r^l}{a^{l+2}}\end{bmatrix}f_l(a)Y_{lm}(\theta,\phi) + \sum_{lm}\begin{bmatrix}0\\ f_l(r)Y_{lm}(\theta,\phi)\end{bmatrix} = s\sum_{lm}f_l(r)Y_{lm}(\theta,\phi). \tag{A 7}$$

The first and second lines of equation (A 7) correspond to $r > a$ and $r < a$, respectively. From this equation we obtain the eigenvalue and the corresponding normalized eigenfunction as

$$s_l = \frac{l}{2l+1}, \tag{A 8}$$

$$\phi_{lm}(\mathbf{r}) = f_l(r)Y_{lm}(\theta,\phi), \tag{A 9}$$

where

$$f_l(r) = \begin{cases} A_l r^l & \text{for } r < a \\ B_l \dfrac{1}{r^{l+1}} & \text{for } r > a, \end{cases} \tag{A 10}$$

$$A_l = \frac{1}{\sqrt{l}a^{l+1/2}},$$

$$B_l = \frac{a^{l+1/2}}{\sqrt{l}}.$$

Here $l = 1, 2, \cdots$; $-l \leqslant m \leqslant l$.

A.2. *Spherical shell inclusion*

For a spherical shell with inner radius a and outer radius b, the eigenfunction can be written as

$$\phi_{lm}(\mathbf{r}) = f_l(r) Y_{lm}(\theta, \phi), \tag{A 11}$$

where

$$f_l(r) = \begin{cases} C_l r^l & r < a \\ \alpha_l r^l + \dfrac{\beta_l}{r^{l+1}} & a < r < b \\ \dfrac{D_l}{r^{l+1}} & r > b. \end{cases} \tag{A 12}$$

From the continuity of $f_l(r)$ on the boundaries of the shell, we have

$$\begin{aligned} C_l a^l &= \alpha_l a^l + \frac{\beta_l}{a^{l+1}} \quad \text{at} \quad r = a, \\ \frac{D_l}{b^{l+1}} &= \alpha_l b^l + \frac{\beta_l}{b^{l+1}} \quad \text{at} \quad r = b. \end{aligned} \tag{A 13}$$

The substitution of equation (A 11) into equation (A 3) yields

$$\frac{l+1}{2l+1}\beta_l \left(\frac{1}{a^{2l+1}} - \frac{1}{b^{2l+1}} \right) = sC_l \quad \text{when} \quad r < a, \tag{A14}$$

$$\frac{l}{2l+1}\alpha_l - \frac{l+1}{2l+1}\frac{\beta_l}{b^{2l+1}} = s\alpha_l$$

$$-\frac{l}{2l+1}a^{2l+1}\alpha_l + \frac{l+1}{2l+1}\beta_l = s\beta_l \quad \text{when} \quad a < r < b, \tag{A15}$$

$$\frac{l}{2l+1}\alpha_l \left(b^{2l+1} - a^{2l+1} \right) = sD_l \quad \text{when} \quad r > b. \tag{A16}$$

It should be noted that (A 13) is not independent from equations (A 14–16). In fact, it can be derived from (A 14–16). This is the case because the boundary conditions are automatically satisfied by the eigenequation (A 3), since the eigenequation comes from the integral representation of Poisson's equation, which already takes into account the boundary conditions. By solving equation (A 15) we get the following eigenvalues:

$$\left.\begin{aligned} s_{l+} &= \frac{1}{2} + \frac{\left[1 + 4l(l+1)\left(\frac{a}{b}\right)^{2l+1}\right]^{1/2}}{2(2l+1)} \\ s_{l-} &= \frac{1}{2} - \frac{\left[1 + 4l(l+1)\left(\frac{a}{b}\right)^{2l+1}\right]^{1/2}}{2(2l+1)} \end{aligned}\right\}. \tag{A17}$$

By back substituting these eigenvalues we solve for the coefficients and represent them as functions of $\beta_{l\pm}$ and $s_{l\pm}$:

$$\left.\begin{aligned} C_{l\pm} &= \beta_{l\pm}\left[\frac{1}{a^{2l+1}} + \frac{l+1}{l-(2l+1)s_{l\pm}}\frac{1}{b^{2l+1}}\right] \\ D_{l\pm} &= \beta_{l\pm}\left[1 + \frac{l+1}{l-(2l+1)s_{l\pm}}\right] \\ \alpha_{l\pm} &= \frac{\beta_{l\pm}}{b^{2l+1}}\left[\frac{l+1}{l-(2l+1)s_{l\pm}}\right] \end{aligned}\right\}. \tag{A18}$$

Here $\beta_{l\pm}$ are determined by normalization of the eigenfunctions:

$$\frac{1}{\beta_{l\pm}^2} = \frac{(2l+1)s_{l\pm}}{a^{2l+1}} + \frac{(l+1)(2l+1)s_{l\pm}\{l+1+2[l-(2l+1)s_{l\pm}]\}}{(l-(2l+1)s_{l\pm})^2 b^{2l+1}}. \tag{A19}$$

The eigenvalues of sphere and spherical shell presented above remain unchanged if we place the sphere at $\mathbf{R}$ and simultaneously changing the spatial variable from $\mathbf{r}$ to $\mathbf{r} - \mathbf{R}$.

Appendix B. Matrix elements of the $\hat{\Gamma}$ operator

From equations (3.34) and (3.35) it is seen that in order to calculate the effective dielectric constant we need to solve a set of linear equations (3.34) to get coefficient A_{iu}. Matrix elements $\Gamma_{iu,jv}$ are needed. These matrix elements are evaluated here along with the matrix elements of z. Appendices C, D are also related to this task. Together they give a self-contained prescription to carry out numerical calculations on DER fluids. While some of the materials might seem detailed and voluminous, they should be helpful to those who want to carry out actual computation. We will consider three different cases: the sphere, the coated sphere and the doubly-coated sphere.

We consider the doubly coated sphere case first. To be specific, we first consider two doubly coated spheres, one located at the origin and the other at $\mathbf{R}$. The inner sphere is denoted by 1, with radius a. The inner shell is denoted by 2, with the inner and outer radii a and b, respectively. The outer shell is denoted by 3, with inner and outer radii b and c, respectiviely. The matrix element is indexed as $\Gamma_{klm,k'l'm'}(-\mathbf{R})$, with k, k' taking the values 1, 2, and 3. The eigenvalue and eigenfunctions required to evaluate the matrix elements are as follows. For the inner sphere, we have

$$s_1, l = \frac{l}{2l+1}, \tag{A 20}$$

$$\phi_{1,lm}(\mathbf{r}) = f_l(r)\, Y_{lm}(\boldsymbol{\Omega}), \tag{A 21}$$

$$f_l(r) = \begin{cases} A_l r^l & \text{when r<a ,} \\ \dfrac{B_l}{r^{l+1}} & \text{when r>a.} \end{cases} \tag{A 22}$$

For the first shell,

$$s_{2,l+} = \frac{1}{2} + \frac{\left[1 + 4l(l+1)\left(\frac{a}{b}\right)^{2l+1}\right]^{1/2}}{2(2l+1)}, \tag{A 23}$$

$$s_{2,l-} = \frac{1}{2} - \frac{\left[1 + 4l(l+1)\left(\frac{a}{b}\right)^{2l+1}\right]^{1/2}}{2(2l+1)}, \tag{A 24}$$

$$\phi_{2,lm\pm}(\mathbf{r}) = f_{2,l\pm}(r)\, Y_{lm}(\Omega), \tag{A 25}$$

where

$$f_{2,l\pm}(r) = \begin{cases} C_{l\pm} r^l & \text{if } r < a \\ \alpha_{l\pm} r^l + \dfrac{\beta_{l\pm}}{r^{l+1}} & \text{if } a < r < b \\ \dfrac{D_{l\pm}}{r^{l+1}} & \text{if } r > b. \end{cases} \tag{A 26}$$

For the outer shell

$$s_{3,l+} = \frac{1}{2} + \frac{\left[1 + 4l(l+1)\left(\frac{b}{c}\right)^{2l+1}\right]^{1/2}}{2(2l+1)}, \tag{A 27}$$

$$s_{3,l-} = \frac{1}{2} - \frac{\left[1 + 4l(l+1)\left(\frac{b}{c}\right)^{2l+1}\right]^{1/2}}{2(2l+1)}, \tag{A 28}$$

$$\phi_{3,lm\pm}(\mathbf{r}) = f_{3,l\pm}(r)\, Y_{lm}(\Omega), \tag{A 29}$$

where

$$f_{3,l\pm}(r) = \begin{cases} E_{l\pm} r^l & \text{if } r < b \\ \gamma_{l\pm} r^l + \dfrac{\delta_{l+}}{r^{l+1}} & \text{if } b < r < c \\ \dfrac{F_{l\pm}}{r^{l+1}} & \text{if } r > c. \end{cases} \tag{A 30}$$

Here $E_{l\pm}$, $\gamma_{l\pm}$, $\delta_{l\pm}$, $F_{l\pm}$ are obtained from $C_{l\pm}$, $\alpha_{l\pm}$, $\beta_{l\pm}$, $D_{l\pm}$ by substituting b as c and a as b in the corresponding expressions. The matrix elements of $\hat{\Gamma}$ can be evaluated from the definition

$$\left.\begin{aligned}\Gamma_{klm;k'l'm'}(-\mathbf{R}) &= s_{k'l'}\int \mathrm{d}V\eta_k(\mathbf{r})\nabla\phi^*_{klm}(\mathbf{r})\cdot\nabla\phi_{k'l'm'}(\mathbf{r}-\mathbf{R})\\ &= s_{k'l'}\int \mathrm{d}\mathbf{S}\cdot\nabla\phi^*_{klm}(\mathbf{r})\phi_{k'l'm'}(\mathbf{r}-\mathbf{R}),\end{aligned}\right\} \tag{A 31}$$

where we have used the fact that $\nabla^2\phi_{klm}(\mathbf{r}) = 0$, which can easily be verified by direct calculation. The integration is over the outwards normal to the surface of the kth grain. When $\mathbf{R} = 0$, the evaluation of these matrix elements is straightforward. When $\mathbf{R} \neq 0$, the expression of the eigenfunctions is substituted into equation (A 31), and then use is made of the following formula, proved in the appendix C:

$$\begin{aligned}&\frac{1}{|\mathbf{r}-\mathbf{R}|^{l'+1}}\int Y^*_{lm}(\Omega_{\mathbf{r}})\,Y_{l'm'}(\Omega_{\mathbf{r}-\mathbf{R}})\mathrm{d}\Omega_{\mathbf{r}}\\ &\quad= (-1)^{l'+m'}\left[\frac{(2l+1)(2l'+1)}{(l+m)!(l-m)!(l'+m')!(l'-m')!}\right]^{1/2}\frac{r^l}{R^{l+l'+1}}\\ &\qquad\frac{(l+l'+m-m')!}{2l+1}P^{m'-m}_{l+l'}(\theta_{\mathbf{R}})\exp[\mathrm{i}(m'-m)\phi_{\mathbf{R}}].\end{aligned} \tag{A 32}$$

After some straightforward though tedious algebraic manipulations, we obtain

$$\begin{aligned}\Gamma_{1lm;1l'm'}(0) &= s^2_{1,l}(2l+1)B_lA_l\delta_{ll'}\delta_{mm'}\\ \Gamma_{1lm;2l'm'\pm}(0) &= s_{1,l}s_{2,l\pm}(2l+1)B_lC_{l\pm}\delta_{ll'}\delta_{mm'}\\ \Gamma_{1lm;3l'm'\pm}(0) &= s_{1,l}s_{3,l\pm}(2l+1)B_lC_{l\pm}\delta_{ll'}\delta_{mm'}\\ \Gamma_{2lm\pm;1l'm'}(0) &= s_{2,l\pm}s_{1,l}(2l+1)C_{l\pm}B_l\delta_{ll'}\delta_{mm'}\\ \Gamma_{2lm\pm;2l'm'\pm}(0) &= s_{2,l\pm}s_{2,l\pm}(2l+1)(\alpha_{1\pm}D_{l\pm}+\beta_{l\pm}C_{l\pm})\delta_{ll'}\delta_{mm'}\\ \Gamma_{2lm\pm;2l'm'\mp}(0) &= s_{2,l\pm}s_{2,l\pm}(2l+1)(\alpha_{l\pm}D_{l\mp}+\beta_{l\pm}C_{l\mp})\delta_{ll'}\delta_{mm'}\\ \Gamma_{2lm\pm;3l'm'\pm}(0) &= s_{2,l\pm}s_{3,l\pm}(2l+1)D_{l\pm}E_{l\pm}\delta_{ll'}\delta_{mm'}\\ \Gamma_{2lm\pm;3l'm'\mp}(0) &= s_{2,l\pm}s_{2,l\mp}(2l+1)E_{l\pm}D_{l\mp}\delta_{ll'}\delta_{mm'}\\ \Gamma_{3lm\pm;1l'm'}(0) &= s_{3,l\pm}s_{1,l}(2l+1)E_{l\pm}B_l\delta_{ll'}\delta_{mm'}\\ \Gamma_{3lm\pm;2l'm'\pm}(0) &= s_{3,l\pm}s_{2,l\pm}(2l+1)E_{l\pm}D_{l\pm}\delta_{ll'}\delta_{mm'}\\ \Gamma_{3lm\pm;2l'm'\mp}(0) &= s_{3,l\pm}s_{2,l\mp}(2l+1)E_{l\pm}D_{l\mp}\delta_{ll'}\delta_{mm'}\\ \Gamma_{3lm\pm;3l'm'\pm}(0) &= s_{3,l\pm}s_{3,l\pm}(2l+1)(\gamma_{l\pm}F_{l\pm}+\delta_{l\pm}E_{l\pm})\delta_{ll'}\delta_{mm'}\\ \Gamma_{3lm\pm;3l'm'\mp}(0) &= s_{3,l\pm}s_{3,l\mp}(2l+1)(\gamma_{1\pm}F_{l\mp}+\delta_{l\mp}E_{l\mp})\delta_{ll'}\delta_{mm'}\end{aligned}$$

and

$$\left.\begin{aligned}
\Gamma_{1lm;1l'm'}(-\mathbf{R}) &= s_{1,l}B_l, s_{1,l'}B_{l'}S(lm,l'm';\mathbf{R})\\
\Gamma_{1lm;2l'm'\pm}(-\mathbf{R}) &= s_{1,l}B_l s_{2,l'\pm}D_{l'\pm}S(lm,l'm';\mathbf{R})\\
\Gamma_{1lm;3l'm'\pm}(-\mathbf{R}) &= s_{1,l}B_l s_{3,l'\pm}F_{l'\pm}S(lm,l'm';\mathbf{R})\\
\Gamma_{2lm\pm;1l'm'}(-\mathbf{R}) &= s_{2,l\pm}C_{l\pm}s_{1,l'}B_{l'}S(lm,l'm';\mathbf{R})\\
\Gamma_{2lm\pm;2l'm'\pm}(-\mathbf{R}) &= s_{2,l\pm}D_{l\pm}s_{2,l'\pm}D_{l'\pm}S(lm,l'm';\mathbf{R})\\
\Gamma_{2lm\pm;2l'm'\mp}(-\mathbf{R}) &= s_{2,l\pm}D_{l\pm}s_{2,l'\mp}D_{l'\mp}S(lm,l'm';\mathbf{R})\\
\Gamma_{2lm\pm;3l'm'\pm}(-\mathbf{R}) &= s_{2,l\pm}D_{l\pm}s_{3,l'\pm}F_{l'\pm}S(lm,l'm';\mathbf{R})\\
\Gamma_{2lm\pm;3l'm'\mp}(-\mathbf{R}) &= s_{2,l\pm}D_{l\pm}s_{3,l'\mp}F_{l'\mp}S(lm,l'm';\mathbf{R})\\
\Gamma_{3lm\pm;1l'm'}(-\mathbf{R}) &= s_{3,l\pm}E_{l\pm}s_{1,l'}B_{l'}S(lm,l'm';\mathbf{R})\\
\Gamma_{3lm\pm;2l'm'\pm}(-\mathbf{R}) &= s_{3,l\pm}E_{l\pm}s_{2,l'\pm}D_{l'\pm}S(lm,l'm';\mathbf{R})\\
\Gamma_{3lm\pm;2l'm'\mp}(-\mathbf{R}) &= s_{3,l\pm}E_{l\pm}s_{2,l'\mp}D_{l'\mp}S(lm,l'm';\mathbf{R})\\
\Gamma_{3lm\pm;3l'm'\pm}(-\mathbf{R}) &= s_{3,l\pm}E_{l\pm}s_{3,l'\pm}D_{l'\pm}S(lm,l'm';\mathbf{R})\\
\Gamma_{3lm\pm;3l'm'\mp}(-\mathbf{R}) &= s_{3,l\pm}E_{l\pm}s_{3,l'\mp}D_{l'\mp}S(lm,l'm';\mathbf{R}),
\end{aligned}\right\} \tag{A 33}$$

where

$$S(lm,l'm';\mathbf{R}) = (-1)^{l'+m'}\left[\frac{(2l+1)(2l'+1)}{(l+m)!(l-m)!(l'+m')!(l'-m')!}\right]^{1/2} (l+l'+m-m')!P_{l+l'}^{m'-m}(\theta_{\mathbf{R}})\exp\left[\mathrm{i}(m'-m)\phi_{\mathbf{R}}\right] \tag{A 34}$$

z_{ilm} can be calculated from the definition

$$z_{ilm\pm} = \int \eta_i \frac{\partial \phi_{ilm\pm}}{\partial z}\mathrm{d}V \tag{A 35}$$

$$= \mathbf{e}_z \cdot \int \eta_i \nabla \phi_{ilm\pm}\mathrm{d}V \tag{A 36}$$

$$= -\mathbf{e}_z \cdot \int \nabla \eta_i \phi_{ilm\pm}\mathrm{d}V. \tag{A 37}$$

Here the integration is over the full space so that the surface contribution is zero in the integration by parts. When $i = 1$, the inner sphere, $\nabla\eta_i = -\delta(r-a)\hat{\mathbf{r}}$ so that

$$z_{1lm} = \mathbf{e}_z \cdot \int \delta(r-a)\hat{\mathbf{r}}\phi_{1lm}\mathrm{d}V \tag{A 38}$$

$$= \int A_l a^{l+2}\cos\theta Y_{lm}(\Omega)\mathrm{d}\Omega \tag{A 39}$$

$$= A_1 a^3\left(\frac{4\pi}{3}\right)^{1/2}\delta_{l1}\delta_{m0}. \tag{A 40}$$

For the inner shell, we have

$$z_{2lm\pm} = \mathbf{e}_z \cdot \int [\delta(r-b) - \delta(r-a)]\hat{\mathbf{r}}\phi_{2lm\pm} \mathrm{d}V$$
$$= (D_{1\pm} - C_{1\pm}a^3)\left(\frac{4\pi}{3}\right)^{1/2} \delta_{l1}\delta_{m0}. \tag{A 41}$$

For the outer shell we get

$$z_{3lm\pm} = (F_{1\pm} - E_{1\pm}b^3)\left(\frac{4\pi}{3}\right)^{1/2} \delta_{l1}\delta_{m0}. \tag{A 42}$$

By limiting k and k' to take values of 1 and 2, we get results for coated spheres. When k, k' are limited only to the value 1, we get results for spheres, and in this case the suffix 1 can be omitted.

Appendix C. Proof of an expansion formula

In this appendix we give the proof of formula (A 32), used in the calculation of the matrix elements of $\hat{\Gamma}$.

The following identity was derived by Danos and Maximon [74]. [See formula (34) in the reference and note that $n_l(x) = \frac{1}{2i}(h_l^{(1)}(x) - h_l^{(2)}(x))$]. In the following we assume $|\mathbf{r}| < |\mathbf{R}|$.

$$n_{l'}(k|\mathbf{r}-\mathbf{R}|)\, Y_{l'm'}(\Omega_{\mathbf{r}-\mathbf{R}}) = \sum_{LM\lambda\mu} i^{\lambda+L-l'}(-1)^{L+m'}[4\pi(2L+1)(2l'+1)(2\lambda+1)]^{1/2}$$
$$\begin{pmatrix} L & l' & \lambda \\ 0 & 0 & 0 \end{pmatrix}\begin{pmatrix} L & l' & \lambda \\ M & -m' & \mu \end{pmatrix} n_L(kR)\, Y_{LM}(\Omega_{\mathbf{R}}) j_\lambda(kr)\, Y_{\lambda\mu}(\Omega_{\mathbf{r}}). \tag{A 43}$$

Here $n_l(x)$, $h_l^{(1)}(x)$ and $h_l^{(2)}(x)$ are respectively the spherical Bessel functions of the second kind (Neumann function) and spherical Hankel functions of the first and second kind. When $kr \ll 1$, we expand both sides of (A 43) and keep the leading terms to obtain

$$-\frac{(2l'-1)!!}{k^{l'+1}|\mathbf{r}-\mathbf{R}|^{l'+1}}\, Y_{l'm'}(\Omega_{\mathbf{r}-\mathbf{R}}) = \sum_{LM\lambda\mu} i^{\lambda+L-l'}(-1)^{L+m'}[4\pi(2L+1)(2l'+1)(2\lambda+1)]^{1/2}$$
$$\begin{pmatrix} L & l' & \lambda \\ 0 & 0 & 0 \end{pmatrix}\begin{pmatrix} L & l' & \lambda \\ M & -m' & \mu \end{pmatrix}$$
$$\left[-\frac{(2L-1)!!}{k^{L+1}R^{L+1}}\right] Y_{LM}(\Omega_{\mathbf{R}})\left[\frac{1}{(2\lambda+1)!!}k^\lambda r^\lambda\right] Y_{\lambda\mu}(\Omega_{\mathbf{r}}). \tag{A 44}$$

By putting all the k-dependent terms together, we have

$$\frac{1}{|\mathbf{r}-\mathbf{R}|^{l'+1}}\, Y_{l'm'}(\Omega_{\mathbf{r}-\mathbf{R}}) = \sum_{LM\lambda\mu} i^{\lambda+L-l'}(-1)^{L+m'}[4\pi(2L+1)(2l'+1)(2\lambda+1)]^{1/2}$$
$$\begin{pmatrix} L & l' & \lambda \\ 0 & 0 & 0 \end{pmatrix}\begin{pmatrix} L & l' & \lambda \\ M & -m' & \mu \end{pmatrix} \frac{k^{\lambda-L+l'}r^\lambda}{R^{L+1}}\frac{(2L-1)!!}{(2\lambda+1)!!(2l'-1)!!}\, Y_{LM}(\Omega_{\mathbf{R}})\, Y_{\lambda\mu}(\Omega_{\mathbf{r}}). \tag{A 45}$$

The left hand side of equation (A 45) is independent of k. In order to have the right hand side also to be k-independent, we must have $\lambda - L + l' = 0$, or $L = \lambda + l'$. Inserting this condition into the formula and knowing the $3j$ symbols to be non-zero only when the sum of the second row is zero, we get

$$\frac{1}{|\mathbf{r}-\mathbf{R}|^{l'+1}} Y_{l'm'}(\Omega_{\mathbf{r}-\mathbf{R}}) = \sum_{\lambda\mu} (-1)^{l'+m'} [4\pi(2\lambda+2l'+1)(2l'+1)(2\lambda+1)]^{1/2} \begin{pmatrix} \lambda+l' & l' & \lambda \\ 0 & 0 & 0 \end{pmatrix} \begin{pmatrix} \lambda+l' & l' & \lambda \\ m'-\mu & -m' & \mu \end{pmatrix} \frac{r^\lambda}{R^{\lambda+l'+1}} \frac{(2\lambda+2l'-1)!!}{(2\lambda+1)!!(2l'-1)!!} Y_{\lambda+l'\,m'-\mu}(\Omega_{\mathbf{R}}) Y_{\lambda\mu}(\Omega_{\mathbf{r}}). \tag{A 46}$$

The explicit expression for the $3j$ symbols in the above special case is given by [75]

$$\begin{pmatrix} \lambda+l' & l' & \lambda \\ 0 & 0 & 0 \end{pmatrix} = (-1)^{l'+\lambda} \left[\frac{(2l')!(2\lambda)!}{(2\lambda+2l'+1)!}\right]^{1/2} \frac{(\lambda+l')!}{l'!\lambda!}, \tag{A 47}$$

$$\begin{pmatrix} \lambda+l' & l' & \lambda \\ m'-\mu & -m' & \mu \end{pmatrix} = (-1)^{(l'-m'-\lambda+\mu)} \left[\frac{(2l')!(2\lambda)!(\lambda+l'+\mu-m')!(\lambda+l'-\mu+m')!}{(2\lambda+2l'+1)!(l'+m')!(l'-m')!(\lambda+\mu)!(\lambda-\mu)!}\right]^{1/2}. \tag{A 48}$$

Multiplying $Y^*_{lm}(\Omega_r)$ on both side of equation (A 46), integrating with respect to $\Omega_{\mathbf{r}}$, and using the orthogonality relation of spherical harmonics

$$\int d\Omega\, Y^*_{lm}(\Omega)\, Y_{\lambda\mu}(\Omega) = \delta_{l\lambda}\delta_{m\mu},$$

we obtain formula (A 32) by substituting equations (A 47) and (A 48) into (A 46).

Appendix D. Ewald sums

In the calculation of the Γ matrix elements, we need to evaluate summations of the form

$$\sigma(L, M) = \sum_{\mathbf{R}} \frac{1}{|\mathbf{R}+\mathbf{r}|^{L+1}} Y_{LM}(\theta, \phi). \tag{A 49}$$

This summation is related to summations over the tensors defined in the following iterative manner. Define the zeroth order tensor

$$T^0 = \frac{1}{|\mathbf{R}+\mathbf{r}|}. \tag{A 50}$$

By successive differentiations with respect to $\mathbf{r}$, we obtain the higher order tensors, the first few being

$$T_i^1 = -\frac{(\mathbf{R}+\mathbf{r})_i}{|\mathbf{R}+\mathbf{r}|^3},$$

$$T_{ij}^2 = \frac{3(\mathbf{R}+\mathbf{r})_i(\mathbf{R}+\mathbf{r})_j}{(\mathbf{R}+\mathbf{r})^5} - \frac{\delta_{ij}}{|\mathbf{R}+\mathbf{r}|^3},$$

$$T_{ijk}^3 = -\frac{15}{|\mathbf{R}+\mathbf{r}|^7}(\mathbf{R}+\mathbf{r})_i(\mathbf{R}+\mathbf{r})_j(\mathbf{R}+\mathbf{r})_k + \frac{3}{|\mathbf{R}+\mathbf{r}|^5}\left[\delta_{ij}(\mathbf{R}+\mathbf{r})_k + \delta_{ik}(\mathbf{R}+\mathbf{r})_j + \delta_{jk}(\mathbf{R}+\mathbf{r})_i\right].$$

The relations to the expressions that appeared on the right hand side of equation (A 49) are as follows:

$$\frac{1}{|\mathbf{R}+\mathbf{r}|^2} Y_{11}(\Omega_{(\mathbf{R}+\mathbf{r})}) = -T_x^1 - \mathrm{i}T_y^1,$$

$$\frac{1}{|\mathbf{R}+\mathbf{r}|^2} Y_{10}(\Omega_{(\mathbf{R}+\mathbf{r})}) = T_z^1,$$

$$\frac{1}{|\mathbf{R}+\mathbf{r}|^3} Y_{22}(\Omega_{(\mathbf{R}+\mathbf{r})}) = T_{xx}^2 - T_{yy}^2 + \mathrm{i}2T_{xy}^2,$$

$$\frac{1}{|\mathbf{R}+\mathbf{r}|^3} Y_{21}(\Omega_{(\mathbf{R}+\mathbf{r})}) = T_{xz}^2 + \mathrm{i}T_{yz}^2,$$

$$\frac{1}{|\mathbf{R}+\mathbf{r}|^3} Y_{20}(\Omega_{(\mathbf{R}+\mathbf{r})}) = \frac{1}{2}T_{zz}^2,$$

$$\frac{1}{|\mathbf{R}+\mathbf{r}|^4} Y_{33}(\Omega_{(\mathbf{R}+\mathbf{r})}) = -[T_{xxx}^3 - 3T_{xyy}^3 + \mathrm{i}(3T_{xxy}^3 - T_{yyy}^3)],$$

$$\frac{1}{|\mathbf{R}+\mathbf{r}|^4} Y_{32}(\Omega_{(\mathbf{R}+\mathbf{r})}) = T_{yyz}^3 - T_{xxz}^3 - \mathrm{i}T_{xyz}^3,$$

$$\frac{1}{|\mathbf{R}+\mathbf{r}|^4} Y_{31}(\Omega_{(\mathbf{R}+\mathbf{r})}) = -(\tfrac{1}{2}T_{zzx}^3 + \mathrm{i}\tfrac{1}{2}T_{zzy}^3),$$

$$\frac{1}{|\mathbf{R}+\mathbf{r}|^4} Y_{30}(\Omega_{(\mathbf{R}+\mathbf{r})}) = -\tfrac{1}{6}T_{zzz}^3.$$

In the following we denote the summation of tensor T as $\tilde{T}$, i.e. $\tilde{T} = \sum_{\mathbf{R}} T$. The evaluation of the zeroth order tensor $\tilde{T}^0$ has been discussed in many standard solid state text books [76, 77], with the result

$$\tilde{T}^0 = \sum_{\mathbf{R}} T^0 = \sum_{\mathbf{R}} \frac{1}{|\mathbf{R}+\mathbf{r}|}\mathrm{erfc}(\eta|\mathbf{R}+\mathbf{r}|) + \sum_{\mathbf{G}} \frac{4\pi}{\nu G^2}\exp(G^2/4\eta^2)\exp(-\mathrm{i}\mathbf{G}\cdot\mathbf{r}), \quad \text{(A 51)}$$

where $\mathbf{G}$ is the reciprocal lattice vectors of lattice $\mathbf{R}$, ν denotes the unit cell volume, and η is a parameter chosen to optimize the convergence. The above summation is intrinsically divergent, so we should try to separate from it the divergent part. If $\mathbf{r} \neq 0$, then the sum over real space lattice points are convergent and the only divergent term comes from $\mathbf{G} = 0$ of the reciprocal sum. So the above equation should be written as

$$\tilde{T}^0 = \sum_{\mathbf{R}} \frac{1}{|\mathbf{R}+\mathbf{r}|} \operatorname{erfc}(\eta|\mathbf{R}+\mathbf{r}|) + \sum_{\mathbf{G}\neq 0} \frac{4\pi}{vG^2} \exp(-G^2/4\eta^2) \exp(-\mathrm{i}\mathbf{G}\cdot\mathbf{r}) + \lim_{g\to 0} \frac{4\pi}{vg^2} - \frac{\pi}{v\eta^2}. \tag{A 52}$$

When $\mathbf{r} = 0$, the proper quantity to be calculated should be

$$\begin{aligned} \sum_{\mathbf{R}\neq 0} \frac{1}{|\mathbf{R}+\mathbf{r}|} = \tilde{T}^0 - \frac{1}{r} &= \sum_{\mathbf{R}\neq 0} \frac{1}{|\mathbf{R}+\mathbf{r}|} \operatorname{erfc}(\eta|\mathbf{R}+\mathbf{r}|) \\ &+ \sum_{\mathbf{G}\neq 0} \frac{4\pi}{vG^2} \exp(-G^2/4\eta^2) \exp(-\mathrm{i}\mathbf{G}\cdot\mathbf{r}) \\ &+ \lim_{g\to 0}\left(\frac{4\pi}{vg^2} - \frac{\pi}{v\eta^2}\right) \exp(-\mathrm{i}\mathbf{G}\cdot\mathbf{r}) + \frac{1}{r}(\operatorname{erfc}(r\eta) - 1). \end{aligned} \tag{A 53}$$

By using the expansion

$$\operatorname{erfc}(x) \approx 1 - \frac{2}{\sqrt{\pi}}x + \frac{2}{\sqrt{\pi}}\frac{x^3}{3} + \cdots,$$

we have

$$\begin{aligned} \sum_{\mathbf{R}\neq 0} \frac{1}{\mathbf{R}} &= \sum_{\mathbf{R}\neq 0} \frac{1}{R} \operatorname{erfc}(\eta\mathbf{R}) + \sum_{\mathbf{G}\neq 0} \frac{4\pi}{\nu G^2} \exp(-G^2/4\eta^2) \exp(-\mathrm{i}\mathbf{G}\cdot\mathbf{r}) \\ &+ \lim_{g\to 0} \frac{4\pi}{vg^2} - \frac{\pi}{v\eta^2} - \frac{2}{\sqrt{\pi}}\eta. \end{aligned} \tag{A 54}$$

By taking derivatives of equation (A 52) with respect to $\mathbf{r}_i$ and using the relation

$$\frac{\partial \operatorname{erfc}(\eta|\mathbf{R}+\mathbf{r}|)}{\partial \mathbf{r}_i} = -\frac{2}{\sqrt{\pi}} \frac{\eta(\mathbf{R}+\mathbf{r})_i}{|\mathbf{R}+\mathbf{r}|} \exp(-\eta^2|\mathbf{R}+\mathbf{r}|^2) \tag{A 55}$$

we get

$$\begin{aligned} \tilde{T}_i^1 &= -\mathrm{i}\sum_{\mathbf{G}\neq 0} \frac{4\pi}{vG^2} G_i \exp(-G^2/4\eta^2) \exp(-\mathrm{i}\mathbf{G}\cdot\mathbf{r}) - \sum_{\mathbf{R}} \operatorname{erfc}(\eta|\mathbf{R}+\mathbf{r}|) \frac{(\mathbf{R}+\mathbf{r})_i}{|\mathbf{R}+\mathbf{r}|^3} \\ &- \sum_{\mathbf{R}} \frac{2\eta}{\sqrt{\pi}} \frac{(\mathbf{R}+\mathbf{r})_i}{|\mathbf{R}+\mathbf{r}|^2} \exp(-\eta^2|\mathbf{R}+\mathbf{r}|^2), \\ \tilde{T}_{ij}^2 &= -\sum_{\mathbf{G}\neq 0} \frac{4\pi}{vG^2} G_i G_j \exp(-G^2/4\eta^2) \exp(-\mathrm{i}\mathbf{G}\cdot\mathbf{r}) \\ &- \sum_{\mathbf{R}} \left(\operatorname{erfc}(\eta|\mathbf{R}+\mathbf{r}|) + \left(\frac{4(\eta|\mathbf{R}+\mathbf{r}|)^3}{3\sqrt{\pi}} + \frac{2\eta|\mathbf{R}+\mathbf{r}|}{\sqrt{\pi}} \right) \exp(-\eta^2|\mathbf{R}+\mathbf{r}|^2) \right) T_{ij}^2 \\ &+ \sum_{\mathbf{R}} \frac{4\eta^2}{3\sqrt{\pi}} \delta_{ij} \exp(-\eta^2|\mathbf{R}+\mathbf{r}|^2) \\ \tilde{T}_{ijk}^3 &= i\sum_{\mathbf{G}\neq 0} \frac{4\pi}{vG^2} G_i G_j G_k \exp(-G^2/4\eta^2) \exp(-\mathrm{i}\mathbf{G}\cdot\mathbf{r}) \end{aligned}$$

$$-\sum_{\mathbf{R}}\left(\operatorname{erfc}(\eta|\mathbf{R}+\mathbf{r}|)+\left(\frac{4(\eta|\mathbf{R}+\mathbf{r}|)^3}{3\sqrt{\pi}}+\frac{2\eta|\mathbf{R}+\mathbf{r}|}{\sqrt{\pi}}\right)\exp(-\eta^2|\mathbf{R}+\mathbf{r}|^3)\right)T^3_{ijk}$$

$$-\sum_{\mathbf{R}}\frac{8\eta^5}{\sqrt{\pi}}\frac{|\mathbf{R}+\mathbf{r}|_i|\mathbf{R}+\mathbf{r}|_j|\mathbf{R}+\mathbf{r}|_k}{|\mathbf{R}+\mathbf{r}|^2}\exp(-\eta^2|\mathbf{R}+\mathbf{r}|^2).$$

Higher order terms can easily be obtained through differentiations.

References

[1] Tao, R., and Roy, G. D. (editors), 1994, *Electrorheological Fluids: Mechanisms, Properties, Technology and Applications* (Singapore: World Scientific).
[2] Bullough, W. A. (editor), 1996, *Electrorheological Fluids, Magnetorheological Suspensions and Associated Technology*, Proceedings of the 5th International Conference (Singapore: World Scientific).
[3] Nakano, M., and Koyama, K. (editors), 1999, *Electrorheological Fluids, Magnetorheological Suspensions and Their Applications*, *Proceedings of the 6th International Conference* (Singapore: World Scientific).
[4] Tao, R. (editor), 2000, *Electrorheological fluids, magnetorheological suspensions and their applications*, *Proceedings of the 7th International Conference* (Singapore: World Scientific).
[5] Tao, R., and Sun, J. M., 1991, *Phys. Rev. Lett.*, **67,** 398.
[6] Bergman, D. J., and Stroud, D., 1992, *Solid State Physics*, Vol. 46 (Academic Press).
[7] Milton, G. W., 1981, *Appl. Phys.* A, **26,** 1207.
[8] Milton, G. W., 1980, *J. appl. Phys.*, **52,** 5286.
[9] Bonnecaze, R. T., and Brady, J. F., 1992. *J. Rheol.*, **36,** 73.
[10] Bonnecaze, R. T., and Brady, J. F., 1992, *J. chem. Phys.*, **96,** 2183.
[11] Klingenberg, D. G., Swol, F. V., and Zukoski, C. F., 1989, *J. chem. Phys.*, **91,** 7888.
[12] Klingenberg, D. J., Swol, F. V., and Zukoski, C. F., 1991, *J. chem. Phys.*, **94,** 6160.
[13] Klingenberg, D. J., 1993, *J. Rheol.*, **39,** 199.
[14] Klingenberg, D. J., Zukoski, C. Z, and Hill, J. C., 1993, *J. appl. Phys.*, **73,** 4644.
[15] Hass, K. C., 1993, *Phys. Rev.* E, **47,** 3362.
[16] Tao, R., and Jiang, Q., 1994, *Phys. Rev. Lett.*, **73,** 205.
[17] Gulley, G. L., and Tao, R., 1997, *Phys Rev.* E, **56,** 4328.
[18] Wang, Z. W., Lin, Z. F., and Tao, R. B., 1996, *Int. J. mod. Phys.* B, **10,** 1153.
[19] Wang, Z. W., Fang, H. P., Lin, Z. F., and Zhou, L. W., 2000, *Phys. Rev.* E, **61,** 6837.
[20] Hu, Y., Glass, J. L., Griffith, A. E., and Fraden, S., 1994, *J. chem. Phys.*, **100,** 4674.
[21] Chen, Y., Sprecher, A. E., and Conrad, H., 1991, *J. appl. Phys.*, **70,** 6796.
[22] Conrad, H., and Sprecher, A. F., 1994, *J. statist. Phys.*, **64,** 1073.
[23] Shih, Y.-H., Sprecher, A. E., and Conrad, H., 1994, *Int. J. mod. Phys.* B, **8,** 2877.
[24] Chen, Y., and Conrad, H., 1994, *Int. J. mod. Phys.* B, **8,** 2895.
[25] Tang, X., Wu, C., and Conrad, H., 1995, *J. Rheol.*, **39,** 1059.
[26] Tang, X., Wu, C., and Conrad, H., 1995, *J. appl. Phys.*, **78,** 4183.
[27] Landau, L. D., and Lifshitz, E. M., 1984, *Electrodynamics of Continuous Media* (New York: Pergamon Press).
[28] Halsey, T. C., and Toor, W., 1990, *Phys. Rev. Lett.*, **65,** 2820.
[29] Wen, W. J., Ma, H. R., Tam, W. Y., and Sheng, P., 1998, *Appl. Phys. Lett.*, **73,** 3070.
[30] Friedberg, R., and Yu, Y. K., 1992, *Phys. Rev.* B, **46,** 6582.
[31] Davis, L. C., 1992, *Appl. Phys. Lett.*, **60,** 319.
[32] Davis, L. C., 1992, *J. appl. Phys.*, **72,** 1334.
[33] Tao, R., Jiang, Q., and Sim, H. K., 1995, *Phys. Rev.* E, **52,** 2727.
[34] Clercx, H. J. H., and Bossis, G., 1993, *Phys. Rev.* E, **48,** 2721.
[35] Ma, H. R., Wen, W. J., Tam, W. Y., and Sheng, P., 1996, *Phys. Rev. Lett.*, **77,** 2499.
[36] Wen, W. J., Ma, H. R., Tam, W. Y., and Sheng, P., 1997, *Phys. Rev.* E, **55,** R1294.

[37] Tam, W. Y., Yi, G. H., Wen, W. J., Ma, H. R., Loy, M. M. T., and Sheng, P., 1997, *Phys. Rev. Lett.*, **78,** 2987.
[38] Martin, J. E., Anderson, R. A., and Tigges, C. P., 1999, *J. chem. Phys.*, **110,** 4854.
[39] Chen, T. J., Zitter, R. N., and Tao, R., 1992, *Phys. Rev. Lett.*, **68,** 2555.
[40] Elliot, M. S., Bristol, B. T. F., and Poon, W. C. K., 1997, *Physica* A, **235,** 216.
[41] Dassanayake, U., Fraden, S., and van Blaaderen, A., 2000, *J. chem. Phys.*, **112,** 3851.
[42] Wen, W. J., Wang, N., Ma, H. R., Lin, Z. F., Tam, W. Y., Chan, C. T., and Sheng, P., 1999, *Phys. Rev. Lett.*, **82,** 4248.
[43] Wen, W. J., Zheng, D. W., and Tu, K. N., 1999, *J. appl. Phys.*, **85,** 530.
[44] Melrose, J. R., 1992, *Mol. Phys.*, **76,** 635.
[45] Melrose, J. R., and Heyes, D. M., 1993, *J. chem. Phys.*, **98,** 5873.
[46] Toor, W. R., 1993, *J. Col. int. Sci.*, **156,** 335.
[47] Martin, J. E., Odinek, J., Halsey, T. C., and Kamien, R., 1998, *Phys. Rev.* E, **57,** 756.
[48] Wen, W. J., Ma, H. R., Tam, W. Y., and Sheng, P., 2000, *Appl. Phys. Lett.*, **77,** 3821.
[49] Li, X. T., and Ma, H. R., 1999, *Acta Phys. Sin.*, **48,** 461.
[50] Li, X. T., and Ma, H. R., 2000, *Acta Phys. Sin.*, **49,** 1070.
[51] Wen, W. J., and Lu, K. Q., 1996, *Appl. Phys. Lett.*, **68,** 3659.
[52] Lan, Y. C., Men, S. Q., Xu, X. Y., and Lu, K. Q., 2000, *J. Phys.* D, **33,** 1239.
[53] Men, S. Q., Xu, X. Y., Lan, Y. C., Xu, S. J., and Lu, K. Q., 2001, *Int. J. mod. Phys.* B, **15,** 788.
[54] Whittle, M., Bullough, W. A., Peel, D. J., and Firoozian, R., 1994, *Phys. Rev.* E, **49,** 5249.
[55] Witten, T. A., and Sandar, L. M., 1981, *Phys. Rev. Lett.*, **47,** 1400.
[56] Wu, C. W., and Conrad, H., 1997, *J. Phys.* D, **30,** 2634.
[57] Wu, C. W., and Conrad, H., 1998, *J. Phys.* D, **31,** 3312.
[58] Wu, C. W., and Conrad, H., 1998, *J. Mar. Res.*, **13,** 3299.
[59] Clercx, H. J. H., and Bossis, G., 1995, *J. chem. Phys.*, **103,** 9426.
[60] Zhao, H. P., Liu, Z. Y., and Liu, Y. Y., 2000, *Solid State Commun.*, **116,** 321.
[61] Halsey, T. C., Martin, J. E., and Adolf, D., 1992, *Phys. Rev. Lett.*, **68,** 1519.
[62] Atten, P., Boissy, C., and Foulc, J. N., 1997, *J. Electrostat.*, **40,** 3.
[63] Hao, T., Kawai, A., and Ikazaki, F., 1999, *Langmuir*, **16,** 3058.
[64] Duan, X. D., Luo, W. L., and Wu, W., 2000, *J. Phys.* D, **33,** 3102.
[65] Choi, H. J., Cho, M. S., Kim, J. W., Kim, C. A., and John, M. S., 2001, *Appl. Phys. Lett.*, **78,** 3806.
[66] Garnett, J. C. M., 1904, *Philos. Trans. R. Soc. London*, **203,** 385.
[67] Sheng, P., 1995, *Introduction to Wave Scattering, Localization, and Mesoscopic Phenomena* (Boston: Academic Press).
[68] Scales, P. J., Grieser, F., Healy, T. W., White, L. R., and Chan, D. Y. C., 1992, *Langmuir*, **8,** 965.
[69] See, H., Tamura, H., and Doi, M., 1993, *J. Phys.* D, **26,** 746.
[70] Anderson, R. A., 1994, *Langmuir*, **10,** 2917.
[71] Zhou, L., Wen, W. J., and Sheng, P., 1998, *Phys. Rev. Lett.*, **81,** 1509.
[72] Severin, J. W., Hokke, R., Vanderwel, H., and deWith, G., 1983, *J. electrochem. Soc.*, **140,** 682.
[73] Briker, C. J., and Scherer, G. W., 1990, *Sol-Gel Science: The Physics and Chemistry of Sol-Gel Processing* (New York: Academic Press).
[74] Danos, M., and Maximon, L. C., 1964, *J. math. Phys.*, **6,** 766.
[75] Landau, L. D., and Lifshitz, E. M., 1987, *Quantum Mechanics*, 3rd edn (New York: Pergamon Press).
[76] Born, M., and Huang, K., 1954, *Dynamical Theory of Crystal Lattices* (Oxford University Press).
[77] Ziman, J. M., 1972, *Principles of the Theory of Solids* (Cambridge University Press).
[78] Wen, W., Zheng, D. W., and Tu, K. N., 1998, *Phys. Rev.* E, **58,** 7682.